Wheel-rail contact models in the presence of switches and crossings

H. Magalhaes, F. Marques, P. Antunes, P. Flores, J. Pombo, J. Ambrósio, A. Qazi, M. Sebes, H. Yin & Y. Bezin

Published online: 01 Mar 2022.

Submit your article to this journal

View related articles

View Crossmark data

IA**VSD**

Taylor & Francis
Taylor & Francis Group

RESEARCH ARTICLE

Check for updates

Wheel-rail contact models in the presence of switches and crossings

H. Magalhaes [a,b], F. Marques [c], P. Antunes [a,b], P. Flores [c], J. Pombo [a,b,d], J. Ambrósio [a], A. Qazi [e,f,g], M. Sebes [e], H. Yin[f] and Y. Bezin [b]

[a]Institute of Railway Research, School of Computing and Engineering, University of Huddersfield, Huddersfield, UK; [b]IDMEC, Instituto Superior Técnico, Universidade de Lisboa, Lisboa, Portugal; [c]CMEMS-UMinho, Departamento de Engenharia Mecânica, Universidade do Minho, Guimarães, Portugal; [d]ISEL, Intituto Politecnico de Lisboa, Lisboa, Portugal; [e]COSYS-GRETTIA, Université Gustave Eiffel, IFSTTAR, Marne-la-Vallée, France; [f]Laboratoire Navier, École des Ponts ParisTech, Univ Gustave Eiffel, CNRS, Marne-la-Vallée, France; [g]ESI Group, Paris, France

ABSTRACT

The development and implementation of wheel-rail contact models in multibody codes are two active research topics, aiming at improving the accuracy of numerical results and computational efficiency of the dynamics analysis. However, the realism of numerical results is challenged when considering switches and crossings (S&C), where the most adverse wheel-rail contact conditions occur. This paper presents a benchmark study where the performance of the multibody codes MUBODyn, VOCO and VI-Rail are assessed using three case scenarios that involve typical contact conditions observed in S&C. A focused description of the relevant methods to determine the wheel-rail contact forces is presented for each software. The three scenarios considered in this work have been designed to represent typical challenging contact conditions observed in S&C, i.e. conformal contact, contact with a sharp edge, and impact loads. The scenarios proposed in this work are fully described, making them easily reproducible. The agreement between results is discussed in the framework of the methods implemented in each code. This work highlights the impact of wheel-rail contact methods on the results as well as on the computational efficiency of the multibody codes.

1. Introduction

The development of computational tools to accurately model the vehicle-track interaction is of utmost importance to design track [1–3], analyse the vehicle performance [4–6], predict damage of components [7–9], or to improve riding characteristics [10–12], just to mention a few. In all cases, the modelling of the wheel-rail interaction, which represents a typical rolling contact problem [13], plays a crucial role. However, the implementation

of wheel-rail contact models in multibody codes involves several challenging issues, some of them related to the description of the contacting surfaces [14,15], the detection of contact zones [16,17] or the computation of the developed forces and moments [18–20]. The validation of wheel-rail contact models has been supported by benchmark exercises that have been performed to compare discrepancies between results of several multibody codes for the same case scenarios. In 1998, the first benchmark for railway vehicles was performed to assess discrepancies that derived mainly from the modelling of the wheel-rail interaction [21]. Other contributions comparing the performance of wheel-rail contact models have been presented [20,22–25], demonstrating the trade-offs between different approaches and highlighting the need for the development of more advanced methodologies to better deal with challenging contact conditions, such as conformal contact. In 2021, the enhancement of multibody codes to address vehicle-track interaction at railway turnouts, i.e. switches and crossings (S&C), has been identified as a key challenge in the international benchmark [26]. This work further investigates the methodologies used in wheel-rail contact models for multibody simulations in S&C focusing on challenging wheel-rail contact configurations.

Turnouts are railway track segments that guide the vehicle in a change from one track to another, hence, they allow to keep the vehicle in the main route or divert its direction. Although these elements represent a small part of the overall railway line, turnouts are associated with a large share of the total maintenance expenses of the railway infrastructure. The existence of variable rail geometry and track flexibility makes the turnout negotiation highly prone to impact loads and to the appearance of unusual wheel-rail contact configurations when compared with regular operations with constant rail profiles [27–29]. The most critical cases occur in the switch, when the wheel transfers from the stock rail to the switch rail, and in the crossing, when the wheel passes from the wing rail to the crossing nose. Therefore, the modelling of wheel-rail contact interaction needs to handle these different contact conditions accurately and efficiently to allow for reliable multibody dynamics simulations of railway vehicles in the presence of S&C.

Several contact modelling methodologies have been developed in recent decades to deal specifically with wheel-rail contact [18,30–32]. One of the most important issues in the development of these computational models deals with the trade-off between accuracy and computational efficiency. Although finite element or boundary element methods accurately determine contact conditions for different wheel-rail configurations [13,33,34], they are computationally expensive and, hence, not adequate for multibody simulations with refined time-step size. Therefore, the utilisation of simplified wheel-rail contact models became widely spread, either by using constraint or elastic approaches. The constraint approach is employed recurring to previously tabulated contact cases, it treats the contact as rigid meaning that no virtual interference or local deformation is considered between the wheel and rail. In this case, a simplified Hertzian contact is often used [35–37]. In turn, the elastic approach assumes that the contacting surfaces can deform locally, with the virtual penetration being the representation of the deformation, which is used for the evaluation of the contact patch area and its pressure distribution [38–43]. Although these models are usually developed based on simplifying assumptions that speed up the calculation procedures, their complexity varies in terms of the geometry of the contacting surfaces, from planar profiles to three-dimensional surfaces, and in terms of the shape of the contact patch, from elliptical to an arbitrary contact.

The wheel-rail contact models proposed in the literature for multibody codes, do not consider the contact conditions typically observed in rails with highly variable cross-sections. These problems mostly occur in the passage of the train through the changing sections of S&C, which can lead to sharp edge contact, widely conformal contact, or impact scenarios [28,44]. The variable rail cross-section requires a parametrised rail profile in the longitudinal position along the track, where the normal contact direction does not lie in the plane of the rail profile, as in the case of the crossing nose. Typically, a set of rail profiles are measured for different track positions, with these values being the input data for the simulation of switch and crossing negotiation. The numerical treatment of this data is required to parametrise the rail geometry at the longitudinal position of the wheels during the dynamic simulation [27,45,46], being the use of polynomial interpolation a standard option [26]. Regarding the wheel-rail contact models, different levels of sophistication might be considered according to the application. When performing turnout geometry and layout optimisation [47,48], simple Hertzian models are usually considered since a tremendous number of simulations are required, with the computational efficiency being a preponderant aspect. More costly contact models are applied for studying turnouts in static cases [49] or generating approximated models [39]. For the study of either vehicle dynamics or the rail damaging phenomena, the utilisation of simplified non-Hertzian contact models presents advantages [8,27,50,51].

The main objective of this work is to evaluate the ability of several wheel-rail contact models, implemented in different software, namely MUBODyn, VOCO and VI-Rail, in handling contact scenarios that typically occur in the negotiation of S&C. Three different idealised running scenarios are utilised as benchmark cases to deal with sharp edge or conformal contacts that typically occur in the switch, and impact cases that take place in the crossing nose. The remainder of the paper is organised as follows: Section 2 summarises the wheel-rail contact methodologies implemented in each of the software tested here; Section 3 presents the three idealised running scenarios, as well as the vehicle and the track models; the main results of the vehicle kinematics and wheel-rail contact forces are compared in Section 4; the main conclusions of this work are outlined in Section 5.

2. Wheel-Rail contact modelling

The multibody codes MUBODyn, VOCO and VI-Rail use different methodologies for the wheel-rail contact modelling. For MUBODyn and VOCO, a more comprehensive description is presented as the authors of this work are also part of the software developers. Less information is presented for the commercial software VI-Rail as the documentation of the software is used as a reference [52]. This section presents an overview of the methods used in the multibody codes, for describing rail geometry, contact detection, contact patch identification, and finding the normal and creep contact forces.

2.1. Handling the variable rail profiles

The parameterisation of the top of the rail, that is, the surface where the wheel is prone to contacting the rail, is required for the multibody simulation. All multibody codes require a set of rail cross sections to create longitudinal polynomials that describe the rail surface. A schematic representation of the approach used in MUBODyn and VI-Rail is depicted in
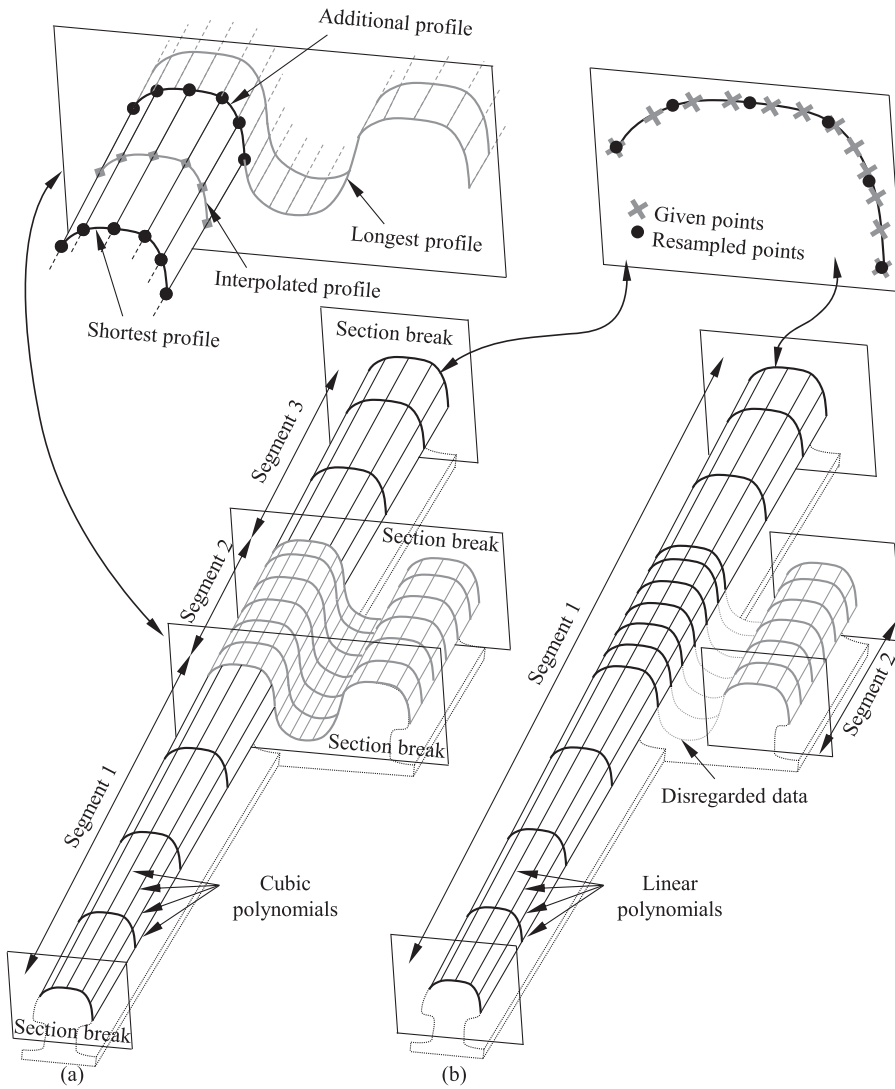
Figure 1. Rail surface parameterisation methodology of: (a) MUBODyn and VI-Rail, (b) VOCO.

Figure 1(a), while the parameterisation considered in VOCO is shown in Figure 1(b). In this case, a rail with variable cross section is considered, comprising two rail heads in the middle.

In MUBODyn and VI-Rail, three rail segments are required to model the complete surface of the rails being different cubic splines used for each one of the segments, as illustrated in Figure 1(a). The section breaks that bounds 'Segment 2' determine sudden cross section variations as one or two rail heads are defined at these longitudinal positions. For modelling purposes, two cross-sections are defined at section breaks, which are the last profile of the previous segment and the first profile of the next segment. In the example highlighted on the top left of Figure 1(a), the section break, set between segments 1 and 2, is shown in detail. Here, the 'Longest profile' profile defines the first profile of segment 2, whereas the
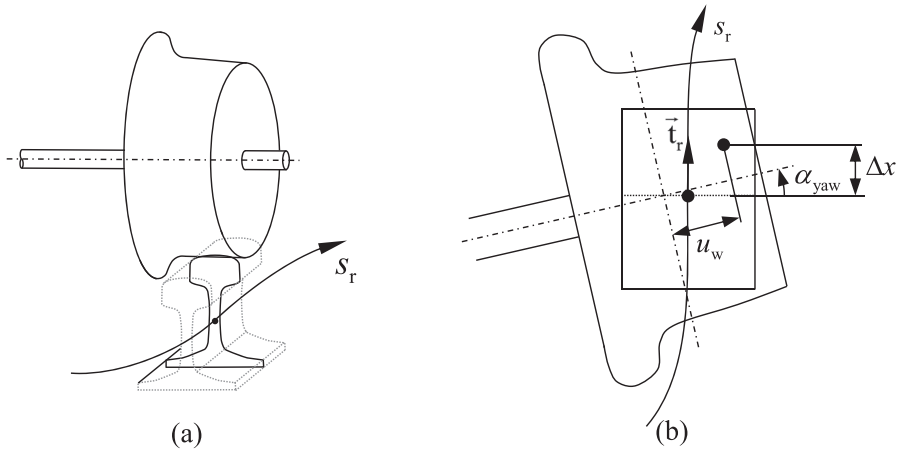
Figure 2. (a) Rail interpolation at the wheel longitudinal position sr. (b) longitudinal shift of the point of contact due to the yaw angle.

last profile of segment 1 is the 'Additional profile', which is derived from the 'Longest profile'. Thus, the rail profile is interpolated at any longitudinal position by using the respective cubic spline, built with 'Cubic polynomials'.

In VOCO, a different approach is used, the rail being represented by two segments as shown in Figure 1(b), one representing the left rail and the other representing the right rail head. Here, part of the cross sections that link the two rail heads is discarded as indicated in Figure 1(b), which is reasonable since the wheel is unlikely to contact that part of the rail. The rail profiles of each segment are resampled so that all cross-section of the same segment is equally refined, enabling the determination of the 'Linear polynomials' for the rail longitudinal direction.

2.2. Contact detection methodology

The contact detection methodology determines pairs of points on the wheel and rail where maximum interference is observed. This step is of utmost importance to determine the contact patch that is discussed in subsection 2.3. MUBODyn and VOCO use different criteria to identify the maximum interference, whereas the method implemented in VI-Rail is based on reference [39]. As the contact detection methodology is not described in detail in the software documentation [52] it is not discussed in this section.

During the dynamic analysis, MUBODyn interpolates the rail profile at the longitudinal coordinate s_r, which is determined by the wheel position at a given time-step, as illustrated in Figure 2(a). As far as VOCO is concerned, after the first linear interpolation described in the previous section, a second linear interpolation of the wheel-rail vertical distance is carried out according to the lateral wheel position. The remaining steps that are presented hereafter are performed under the assumption that the rail cross-section is locally straight and invariant. In the case of VOCO, the yaw relative motion is ignored, hence the interference between the wheel profile and rail profile is purely solved in a 2D plane. In the case of MUBODyn, the methodology proposed in [17] is used, which accounts for the roll
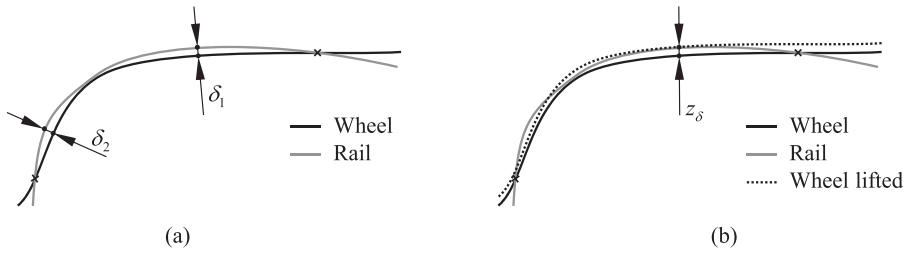
Figure 3. Interference assessment (a) in MUBODyn is normal to the wheel and rail surfaces (b) and in VOCO is vertical.

and yaw relative motion between the wheel, meaning that, although the rail is interpolated at a specific longitudinal coordinate, the main point of contact may occur before or after the interpolated rail cross section, as indicated in Figure 2(b) with dimension Δx.

In MUBODyn, the interference is assessed normal to the wheel and rail surfaces and determined at all maxima solutions, i.e. maximum indentation. Figure 3(a) shows a case in which the two pairs of contact points are identified by the penetrations δ_1 and δ_2, which are obtained through an optimisation procedure, which accounts for the most significant computation cost in the wheel-rail contact method for MUBODyn [17]. In VOCO, the interference is assessed directly from the vertical geometric separation between the wheel-rail profiles, and projected onto the tangent plane.

2.3. Contact patch determination

Different multibody codes define the penetration function differently, that is, the distance between the wheel and rail at the interfering regions, which is required to determine the contact patch. In MUBODyn, the penetration function is defined with respect to the contact patch reference by the pair of points where maximum penetration is observed, as illustrated in Figure 3. The contact patch is determined based on a fraction of the inter-penetration, namely 1-ϵ as shown in Figure 4(a), meaning that a local elastic deformation due to the wheel-rail contact forces is considered. Here, ϵ is set to 0.55 as suggested in [39] and as implemented in [20]. Therefore, a single interference might lead to multiple contact patches, as illustrated in Figure 4. Here, numerical instabilities related to the split of a contact patch or union of separate patches, are mitigated by the extended Kik-Piotrowski model proposed in [53]. The contact patch is then determined based on the penetration function. In MUBODyn, the length of each strip is obtained according to the relation proposed in the Kik-Piotrowski method [39], which is illustrated in Figure 5(a). In this work, MUBODyn determines an equivalent elliptical contact patch where the semi-axis a and b are determined to match the contact patch area and the width of the original non-Hertzian contact patch, as shown in Figure 5(a).

In VOCO, the semi-Hertzian STRIPES method is used. The whole interference between the wheel and rail is used to determine the contact patch, where the penetration function is defined as [38]:
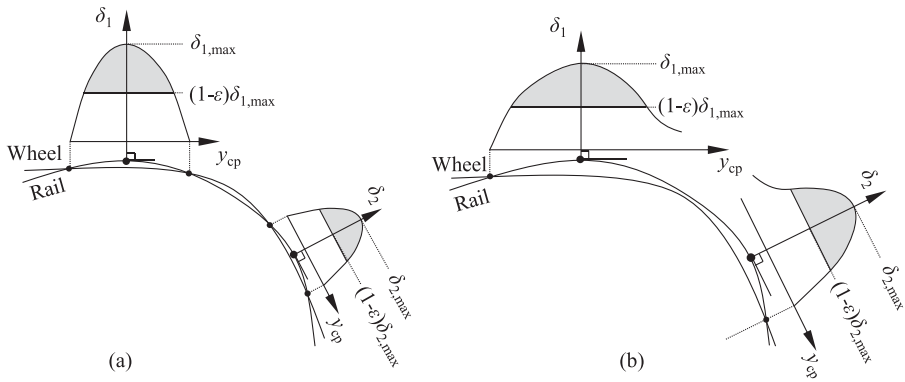
$$\delta_i = (z_\delta - z_i)\cos(\gamma_i) \tag{1}$$

Figure 4. Separation function of two contact patches when (a) two independent and (b) single interferences occur.
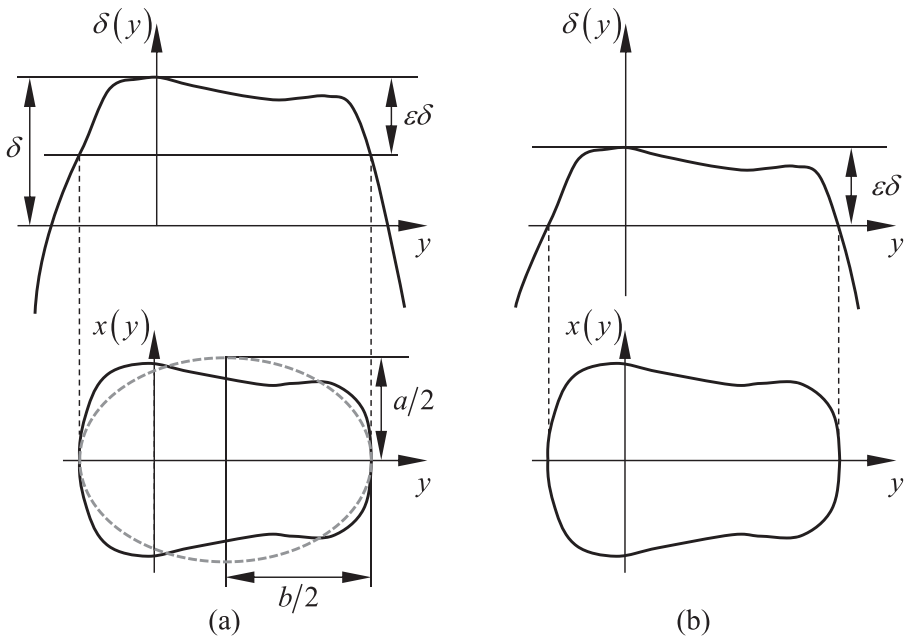

Figure 5. Schematic representation of the penetration function and contact patch for (a) MUBODyn and for (b) VI-Rail.

where z_δ, z_i and γ_i are the vertical penetration depth, the vertical distance between the 'Wheel lifted' and the 'Rail' profile in geometric contact at strip i, and the contact angle of a strip i on the rail profile, respectively, as shown in Figure 3(b). A given strip i is in contact if δ_i is positive [38]. The maximum value δ_{max} in VOCO corresponds to the penetration depth $\epsilon\delta$ as used in [39], but with a different expression for ϵ [54]. This expression of ϵ depends on the local properties of each strip [38]. However, neither the approach δ nor ϵ are explicitly assessed in STRIPES. VI-Rail also defines the contact patch based on the whole

wheel-rail interference as shown in Figure 5(b), which is equivalent to a figure presented in the documentation [52] for which a more detailed description is not available.

2.4. Normal contact impact

The formulation to determine the normal contact force used in MUBODyn, VOCO and VI-Rail differ significantly. In MUBODyn, the Hertz-based model that accounts for some energy dissipation in the contact, via the restitution coefficient is used, which is written as [17]:

$$F_n = \begin{cases} K\delta^n c_e & \dot{\delta} \leq -v_0 \\ K\delta^n[c_e + (1 - c_e)(3r^2 - 2r^3)] & -v_0 < \dot{\delta} < v_0 \\ K\delta^n & \dot{\delta} \geq v_0 \end{cases} \tag{2}$$

where the transition parameter is $r = (\dot{\delta} + v_0)/2v_0$, K is the generalised contact stiffness that depends on the wheel-rail contact conditions, δ is the maximum virtual penetration of a contact patch, as shown in Figure 3(a), and $\dot{\delta}$ is its the first time derivative, n defines the degree of nonlinearity, typically 1.5 for wheel-rail contact, c_e is the restitution coefficient, and v_0 is the penetration velocity tolerance, generally set to 0.1 m/s.

In VOCO, the total lateral and vertical forces Y and Q are the sums of normal and tangent forces f_{ni} and f_{ti} at each strip:

$$\begin{cases} Y = \sum_i f_{ti} \cos \gamma_i - f_{ni} \sin \gamma_i \\ Q = \sum_i f_{ni} \cos \gamma_i + f_{ti} \sin \gamma_i \end{cases} \tag{3}$$

The normal forces are assessed at the strip level by the semi-Hertzian method [38] with:

$$f_{ni} = k_i \delta_i \tag{4}$$

$$k_i = \frac{E}{2(1 - v^2)} \frac{1 + A_i/B_i}{n_i^3} \Delta y_i \tag{5}$$

where δ_i is the penetration of strip i, E is Young modulus, μ is the Poisson ratio, A_i and B_i are local longitudinal and lateral curvatures, respectively, Δy_i is the width of the strip i, n_i is the Hertzian coefficient used for the evaluation of the lateral semi-axis b, which is a function of A_i/B_i. The stiffness k_i is pre-tabulated as a function of the lateral position of the wheel with respect to the rail, and the curvilinear track position [1]. In equation (5) k_i depends on local properties, thereby a smoothing of the B curvature is required beforehand in order to avoid sharp variations [38]. An undesired effect of this smoothing has consequences that are later discussed in the results section. The creep forces are expressed with a variant of FASTSIM described in section 2.5. The wheel dynamics is conditioned considering the spring stiffness $K_{y,z}$ and the damping coefficients $C_{y,z}$ in the vertical and lateral directions,

$$\begin{cases} Y = -K_y(y_w - y_r) - C_y(\dot{y}_w - \dot{y}_r) \\ Q = -K_z(z_w - z_r)^{3/2} - C_z(\dot{z}_w - \dot{z}_r) \end{cases} \tag{6}$$
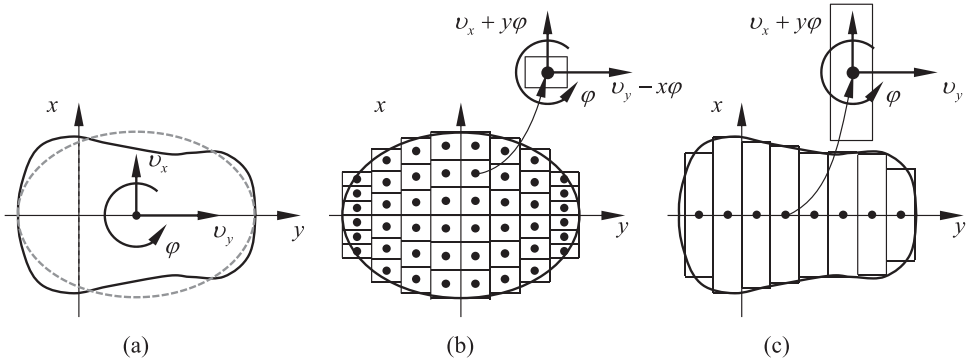
Figure 6. Creepage assessed at the (a) centre of the contact patch, (b) at each cell of a discretized contact patch and (c) at each strip of a contact patch.

where y_w, y_r, z_w and z_r are the lateral and vertical position of the wheel and rail at the mean contact level. Within the scope of the benchmark, a typical value of the Hertzian stiffness, K_z, of 70 GN/m$^{3/2}$ is used, which can be obtained from [55]:

$$K_z = \frac{2}{3} r^{2/3} \frac{E}{1 - \nu^2} \frac{1}{\sqrt{A + B}} \qquad (7)$$

where r is here the Hertzian coefficient used to assess the rigid approach, whereas K_y is set equal to 500 kN/mm. In both directions, a damping of 20000 Ns/m is considered to not overestimate the dissipative effect. The values of stiffness and damping are assessed heuristically.

Although the Kik-Piotrowski model is used in VI-Rail documentation [52], which disregards any dissipative term on the normal contact [39], a parameter named as 'Hertzian damping ratio' is found in the input files, which affects the normal contact forces when impact loads are observed. Therefore, the normal contact force predicted in VI-Rail also depends on the speed of penetration, but the implemented model is not disclosed.

2.5. Creep forces

The creep forces are determined based on the longitudinal and lateral creepages, υ_x and υ_y, and spin creepage, φ, of the contact patch. The main difference between the three multibody codes is that MUBODyn uses global creepages, that is, creepages at the point where maximum penetration occurs, as shown in Figure 6(a), whereas VI-Rail discretizes the contact patch into cells and assess the creepages at the centre of each cell, as shown in Figure 6(b). In VOCO, the contact patch is discretised using strips, in each one of which the creepages are defined, as shown in Figure 6(c). Thus, the Polach Method [56] is used in MUBODyn, while VI-Rail uses FASTSIM, as presented in [52], VOCO uses a functional approximation of FASTSIM adapted for non-elliptical contact patches by using the local properties of each strip [38,57].
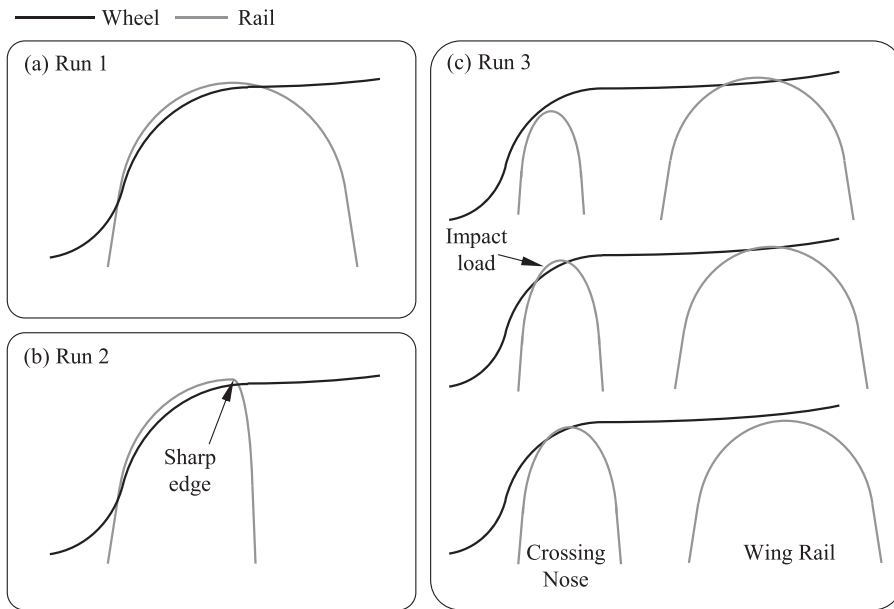
Figure 7. Schematic representation of: (a) a wheel-rail conformal contact; (b) a contact between the wheel and a rail sharp edge; (c) impact load in the crossing nose.

3. Simulation cases

A set of three running scenarios are designed to analyse the performance of the different multibody software presented in the previous section. The three railway dynamics simulations cases, which are hereafter named as 'Run 1', 'Run 2' and 'Run 3', were defined iteratively through parameterised models, so that specified contact conditions occur, which are typical in S&C. 'Run 1' and 'Run 2' enable to reach two wheel-rail contact conditions, typically observed when the vehicle negotiates a diverging route through a switch. In 'Run 1', the cross sections of both wheel and rail are defined to achieve a large and conformal contact as depicted in Figure 7(a). In 'Run 2', the rail cross section is defined to represent an intermediate profile of the switch rail comprising a sharp edge that results from the machining in the inner side of the switch rail leading to a very small radius of curvature, as shown in Figure 7(b). Thus, the wheel contacts the sharp edge promoting a contact condition for which the most common wheel-rail contact models are challenged. 'Run 3' is used to investigate the impact at the crossing nose when the wheel load is transferred from the wing rail to the crossing nose, as schematically represented in Figure 7(c) with three consecutive conditions from top to bottom. To ensure that the contact conditions represented in Figure 7 effectively occur, curved tracks are considered for both 'Run 1' and 'Run 2', whereas a tangent track is used in 'Run 3'. For all cases, a simple bogie model running at 100 km/h is considered. A thorough description of the three simulation cases is presented to allow the interested reader to reproduce them, namely in what concerns the vehicle model, track model, and profiles parametrization. The values of the model parameters are presented in the tables shown in Appendix A.
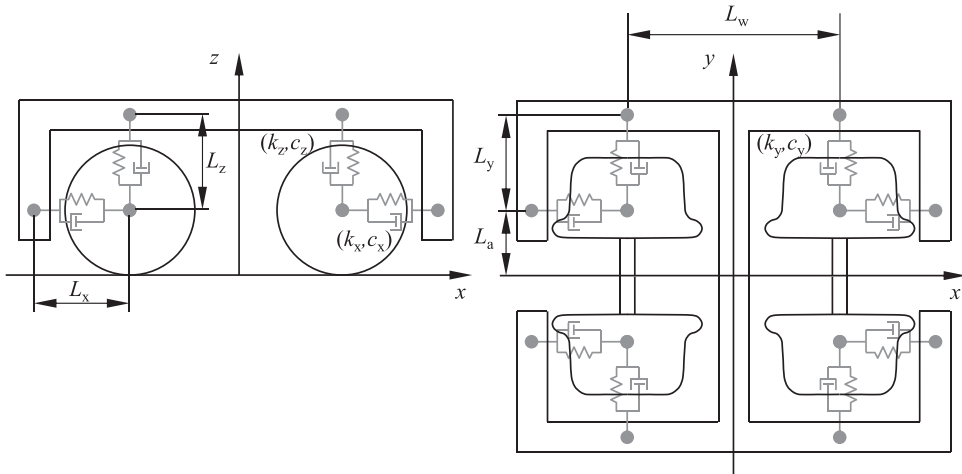
Figure 8. Schematic representation of lateral and top views of the bogie model.

3.1. Bogie model

The bogie model comprises a bogie frame supported by two wheelsets through the primary suspension as depicted in Figure 8. The parameters used for this model based on the Manchester passenger vehicle are listed in Table 2 [58]. The main differences between the model used here and that in the Manchester benchmark are that only half of the carbody mass is considered as part of the bogie frame, and the series stiffness of the primary suspension elements are removed. Note that, in the initial conditions, the bogie frame weight is supported by the pre-load of the vertical springs to achieve vertical equilibrium and, therefore, the undeformed length of these springs is higher than its mounted length as it is listed in Table 2.

3.2. Track model

A curved track with null cant is considered for both 'Run 1' and 'Run 2'. The horizontal curvature of the track is schematically depicted in Figure 9(a), in which a positive curvature represents a left curve. This track comprises a tangent segment followed by a curve transition and by a curve with a constant radius of 245 m matching the GB case of the S&C Benchmark [26]. The curve transition is 25 m long with linearly increasing curvature. The results presented for both 'Run 1' and 'Run 2' are obtained for a 35 m track section that starts from 5 m before the transition curve and ends 5 m after it, as indicated in Figure 9(a). For 'Run 3', a tangent track is considered in which a crossing is placed on its right side. Here, the simulation results are presented for a 10 m track section, which starts 5 m before the crossing nose. More details on the crossing element layout are found in section 3.5.

The co-running model shown in Figure 9(b) is used in all simulations cases to represent the track dynamics, which is a lumped parameter model with three mass elements, two of them represent the left and right rails and the other mass represents a section of the sleeper-ballasted layers. Lateral and vertical spring and dampers elements are used to connect the rails to the sleeper-ballast and the sleeper-ballast to the track foundation, as shown in Figure 9(b). Note that all mass elements have planar motion, i.e. they can move
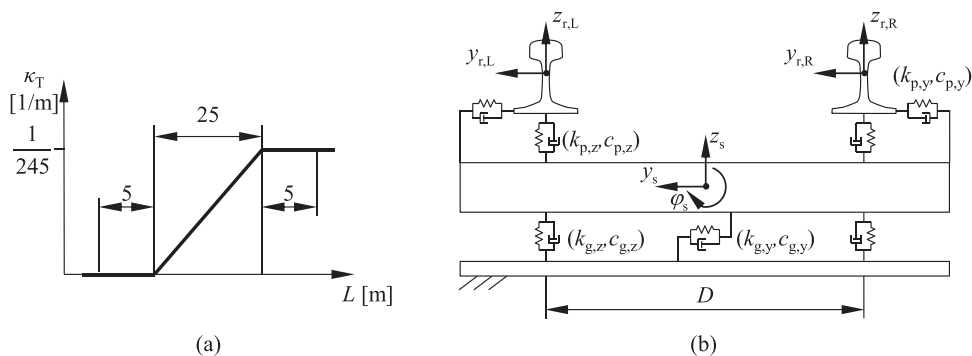
Figure 9. (a) Track curvature for both 'Run 1' and 'Run 2' and (b) co-running model.

laterally and vertically, and the sleeper-ballast can also exhibit roll motion, that is, rotate around the longitudinal axis. The parameters of the co-running model are listed in Table 3, being the same for all cases.

3.3. Wheel profile parameterization

The wheel profile is defined by three pieces of ellipses, as depicted in Figure 10. Each ellipse is defined by the two semi-axes a_i and b_i where i corresponds to 'T' for the tread, 'C' for the concave part, and 'F' for the flange. The union between ellipses always ensures the continuity of the first derivative. In the tread-concave union, the profile slope is null and, in the flange-concave union, the slope is prescribed by the specified value df_w. Also, the lateral coordinate of the tread-concave union is defined by u_0 relatively to the wheel profile origin, as shown in Figure 10. The wheel profile is described by a set of points that are equally spaced over its arc-length with a distance of Δs_w. The same wheel profile geometry is considered for all running scenarios represented in this work, with the required parameters are listed in Table 4.

3.4. Rail profile parameterization

The rail profiles are parametrised by two ellipses that represent the head of the rail, and two straight lines that represent the lateral faces, as depicted in Figure 11, in which the continuity of the first derivative is ensured by this parameterisation. Each ellipse describes one side of the rail, meaning that the highest point of the rail profile is at coordinate $u_r = 0$ and its slope is null. The two straight lines, defined by their slopes, are tangent to the corresponding ellipses, hence the slope parameters limit the width of the ellipses. The length of the straight lines measured in the horizontal direction are defined by the parameters Δu_L and Δu_R for the left and right sides, respectively, as displayed in Figure 11. A parameter f_0 can be used to adjust the vertical coordinate of the rail profile. The rail profile is described by a set of points that are equally spaced over its arc-length with distance Δs_r. Note that this parametrization allows describing asymmetric rail profiles which is required in the design of the contact scenarios considered in this study.
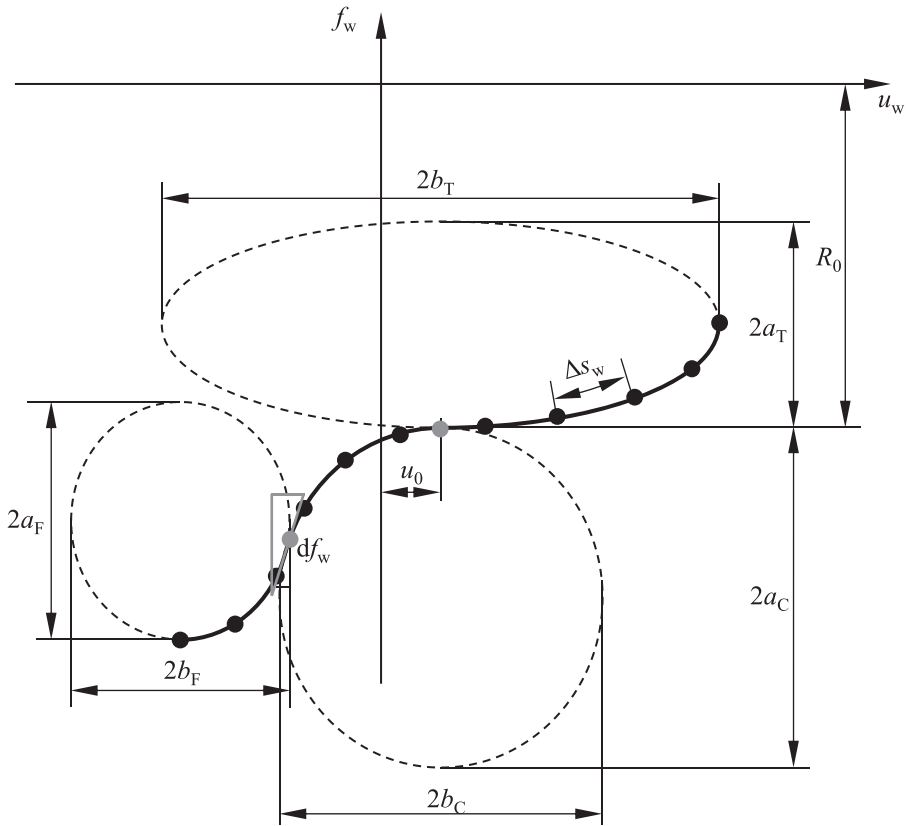
Figure 10. Schematic representation of the wheel profile parametrization.

The rail profiles used in Runs 1, 2 and 3 are described in Table 5. In 'Run 1', the left and right rail profiles have the same geometry. In 'Run 2', the left and right rails are different for b_R, which is 1 mm to make the ellipse thin, which enables to represent the sharp edge depicted in Figure 7(b). In the case of 'Run 3', the rail profile of 'Run 1' is used with the exception of the crossing panel where a variable rail profile is considered as described in section 3.5.

3.5. Crossing layout parameterization

The crossing rail comprises the wing rail and the crossing nose, whose cross sections are parametrised through ellipses and straight lines. The top and lateral views of the crossing are schematised in Figure 12, where three longitudinal coordinates of the right rail are identified as '1', '2' and '3' that refer to the three cross sections represented in Figure 13. The wing rail deviates laterally in the interval between position '1' and '3' according to the crossing angle α. Note that within this interval the wing rail profile is wider than the one observed at position '1' by a factor of $1/\cos(\alpha)$ due to the projection of the rail cross section onto the transverse plane of the track. The first cross section of the crossing nose is defined at position '2', as shown in Figure 13. From position '2' up to position '3', the rail cross section varies linearly until reaching the original cross section observed at position
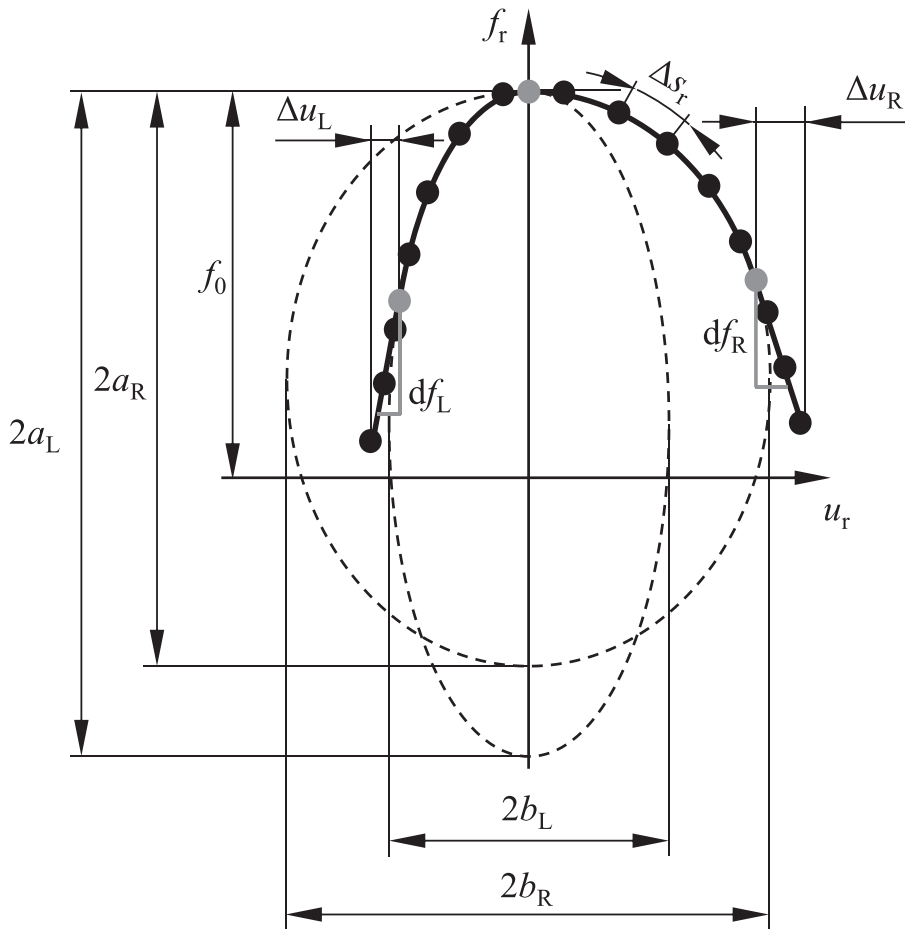
Figure 11. Schematic representation of the rail profile parameterisation.

'1'. Note that the angle β enables the representation of the ramp that is observed in a real crossing nose, which elevates the rail cross section linearly as demonstrated in Figure 12. The gap between the crossing nose and the wing rail is defined by parameter c, which represents the distance between the inner sides of the ellipses that define those two rail profiles as exhibited in Figure 13. It is highlighted that, in this parametrization, the ellipses that define the wing rail at position '1' and the crossing nose at position '2' and '3' are aligned to the left, as shown in Figure 13. Note also that a straight line is considered to connect the wing rail and the crossing nose, which is convenient for the rail interpolation methodology employed in MUBODyn and Vi-Rail. Note that the profiles are discretized in a set of equally spaced points over their arc-length.

4. Results of the benchmark

Selected results obtained with MUBODyn, VOCO and VI-Rail for 'Run 1', 'Run 2' and 'Run 3' are presented, in this section, with the aim of identifying the impact of the methods implemented in the three multibody codes. The focus is put on the right wheels of the
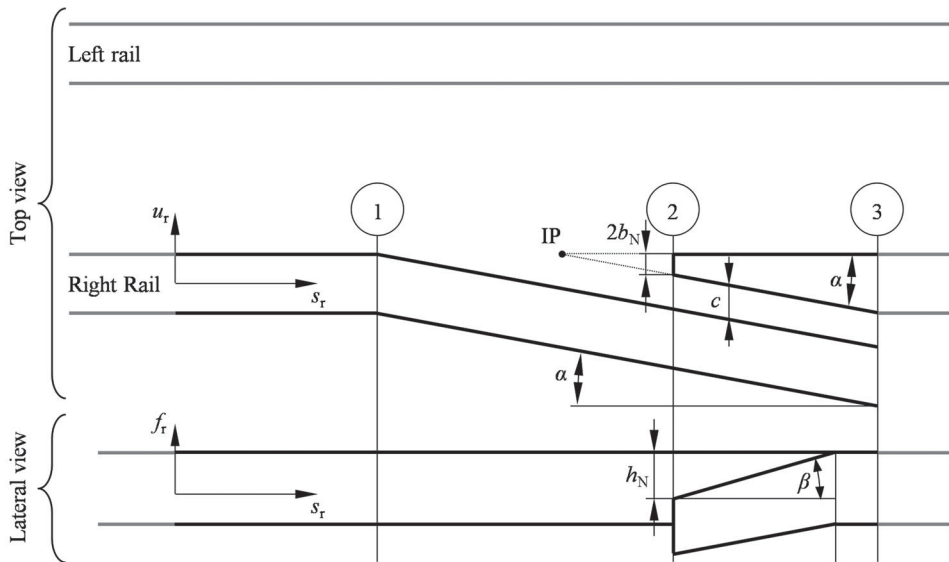
Figure 12. Crossing layout parameterisation.

bogie, which negotiate the outer rails of 'Run 1' and 'Run 2', and the crossing element of 'Run 3'.

4.1. Run 1 – conformal contact

The objective of this case study is to analyse contact patches that show the largest contact area, which are expected at the outer rails where the contact flange occurs. Figure 14 shows the area of the contact patches during the curve transition for the (a) trailing and (b) leading outer wheels. The largest contact area is observed for the trailing wheelset that exceeds 140 mm^2, in the case of MUBODyn. Figure 14(a) demonstrates that VOCO and VI-Rail have significant differences, with a systematically higher contact area obtained with VI-Rail, while MUBODyn reaches good agreement with both VOCO and VI-Rail in particular intervals, namely where peaks and troughs are observed. In what concerns the contact areas of the leading outer wheel, a good agreement is obtained between MUBODyn and VOCO for the smaller contact patch and between MUBODyn and VI-Rail for the larger contact patch, as shown in Figure 14(b).

The contact position at the wheel and rail is shown in Figure 15(a, b), respectively. Note that different criteria are used to determine the contact position on the wheel and rail. MUBODyn defines the contact points as the location where the maximum penetration is observed at each contact patch, and the condition that the interference is normal to the wheel and rail surfaces must be verified, as shown in Figure 3(a). In VOCO, the contact position is a weighted sum using the normal force per strip as the weight. No precise definition has been found for VI-Rail, but it seems similar to that of MUBODyn. From the results, it is observed that VOCO shows lower amplitude variation for the contact position when compared to MUBODyn and VI-Rail.
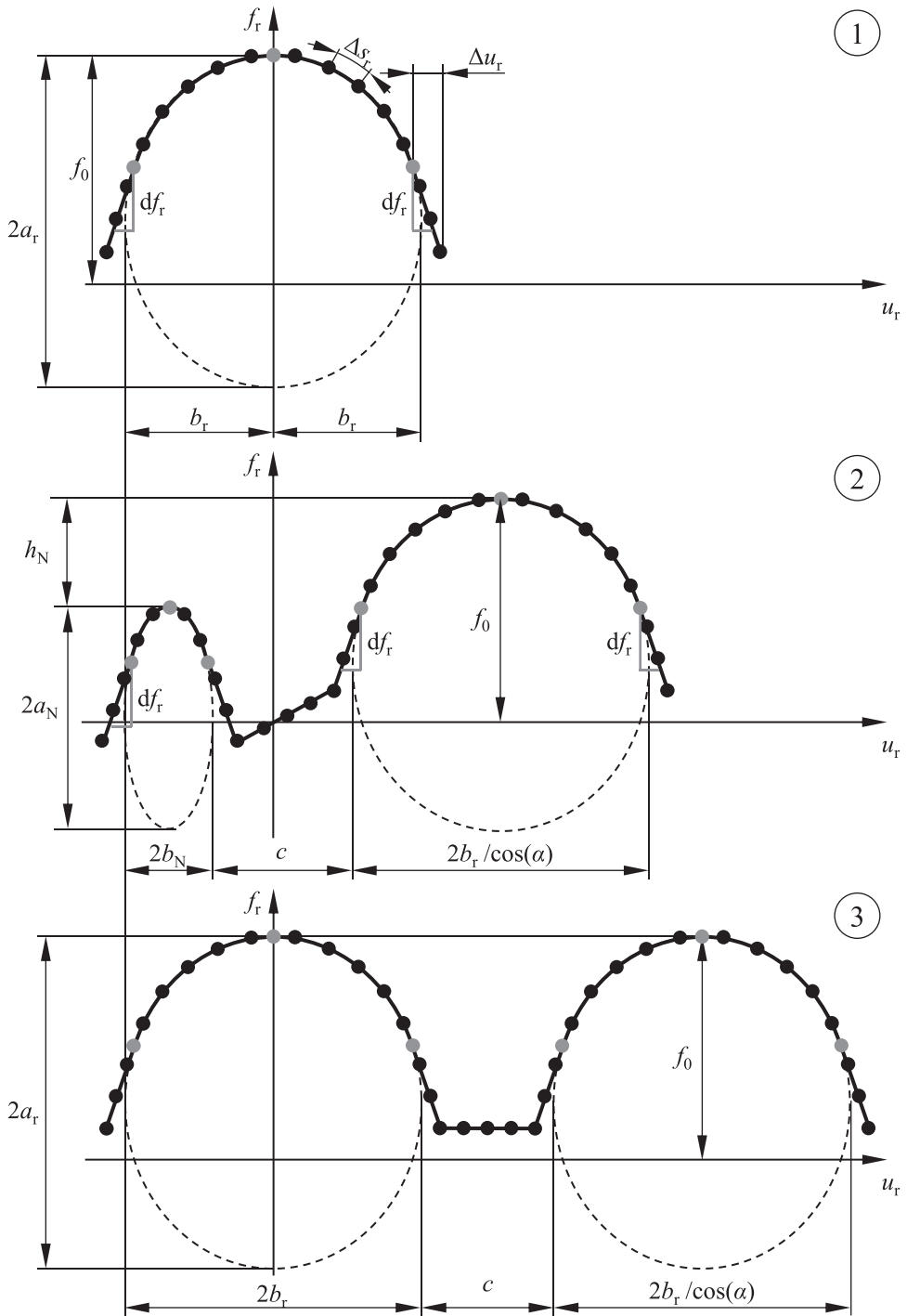
Figure 13. Cross sections of the crossing at position '1', '2' and '3' as indicated in Figure 12.
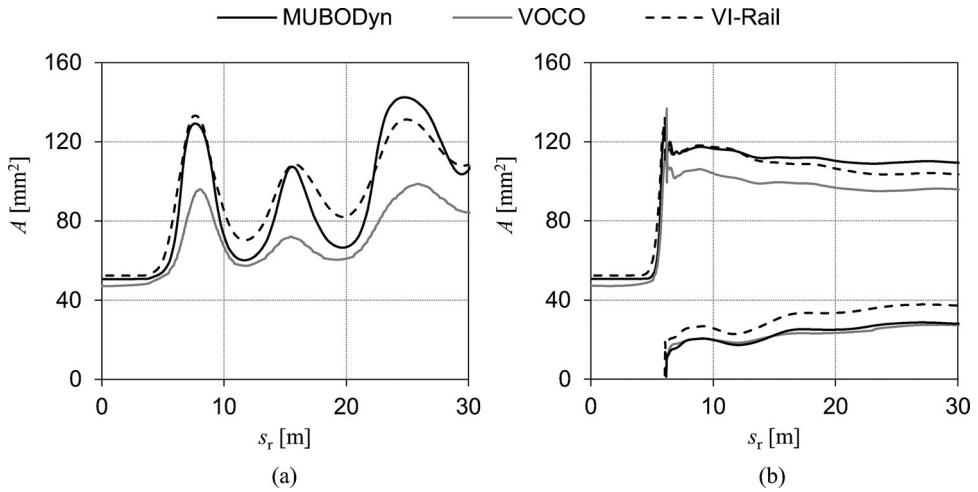
Figure 14. Contact area of the contact patches observed in the outer (a) trailing and (b) leading wheels.
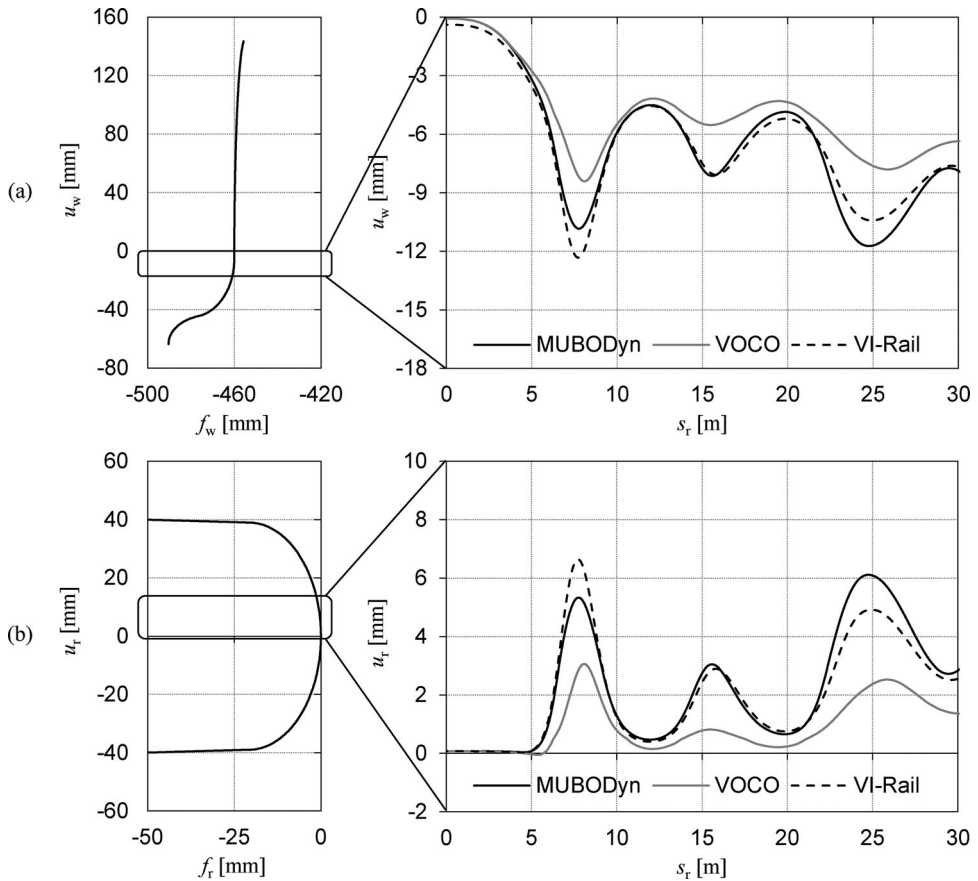

Figure 15. Left hand side: (a) Wheel and (b) rail profiles. Right hand side: corresponding position of the contact patch for the trailing outer wheel-rail pair.

Additionally, the shape of the contact patch of the outer trailing wheel is obtained for the trailing wheel when it reaches the beginning and end of the curve transition, that is, at s_r equal to 0 and 25 m shown in Figure 16. Here, VI-Rail is not considered as this contact shape is not available to the user. The contact patches obtained with CONTACT [59], which is a software based on the Kalker rolling contact theory used as a reference for other simplified methods [60], are also presented. CONTACT requires the separation function and normal contact force as inputs, which are obtained with MUBODyn and VOCO. An elliptical contact shape is observed at $s_r = 0$ m and a good agreement is recognised between MUBODyn, VOCO and CONTACT, as shown in Figure 16(a–c). The elliptical shape is expectable as the contact point is observed at the origin of the wheel and rail, as shown in Figure 15, where the curvatures are locally constant, approximately. Wider contact patches are observed at the end of the curve transition, as shown in Figure 16(b–d), where the contact patches deviate from the elliptical shape. MUBODyn and CONTACT show a good agreement, whereas VOCO slightly underestimates the contact patch area when compared with CONTACT. The contact patches obtained with MUBODyn and VOCO differ as the contact conditions predicted at this instant of the simulation are also different as shown in Figure 14(a). In this conformal configuration, a slight difference in the lateral displacement of the wheel induces a comparatively high difference in the contact patch and location.

The contact forces at the contact patch of the outer trailing wheelset are displayed in Figure 17 and show a good agreement. In what concerns the normal contact forces, a better match is recognised between MUBODyn and VI-Rail, whereas VOCO obtains slightly lower peaks, which agrees with the smaller contact patch presented in Figure 14(a). Regarding the longitudinal and lateral creep forces, a general good agreement is observed between the three multibody codes.

One cause for the discrepancies between the multibody codes is the difference in the contact detection methodology implemented in VOCO that neglects the yaw relative motion, the method implemented in VI-Rail being unknown to the authors. Another source of discrepancy comes from the determination of the penetration function and its conversion into a contact patch, where MUBODyn uses a portion of the penetration function, VOCO virtually interpenetrates the wheel vertically and although the methods used in VI-Rail are not publicly available they seem to differ from those used in MUBODyn and VOCO.

4.2. Run 2 – contact sharp edge

In this case study, the focus is put on the contact patch at the sharp edge, which is observed in the trailing outer wheel. The contact position at the wheel and rail surface is shown in Figure 18. Here, a better agreement is also observed between MUBODyn and VI-Rail during most of the simulation, which indicates that the criteria to define the contact position might be similar, whereas VOCO shows higher oscillation of the contact position, which is caused by the presence of the sharp edge.

The contact patches obtained with MUBODyn and VOCO at the beginning and end of the curve transition, that is, at s_r equal to 0 and 25 m respectively, are shown in Figure 19 as well as the contact patches obtained with CONTACT where the separation function
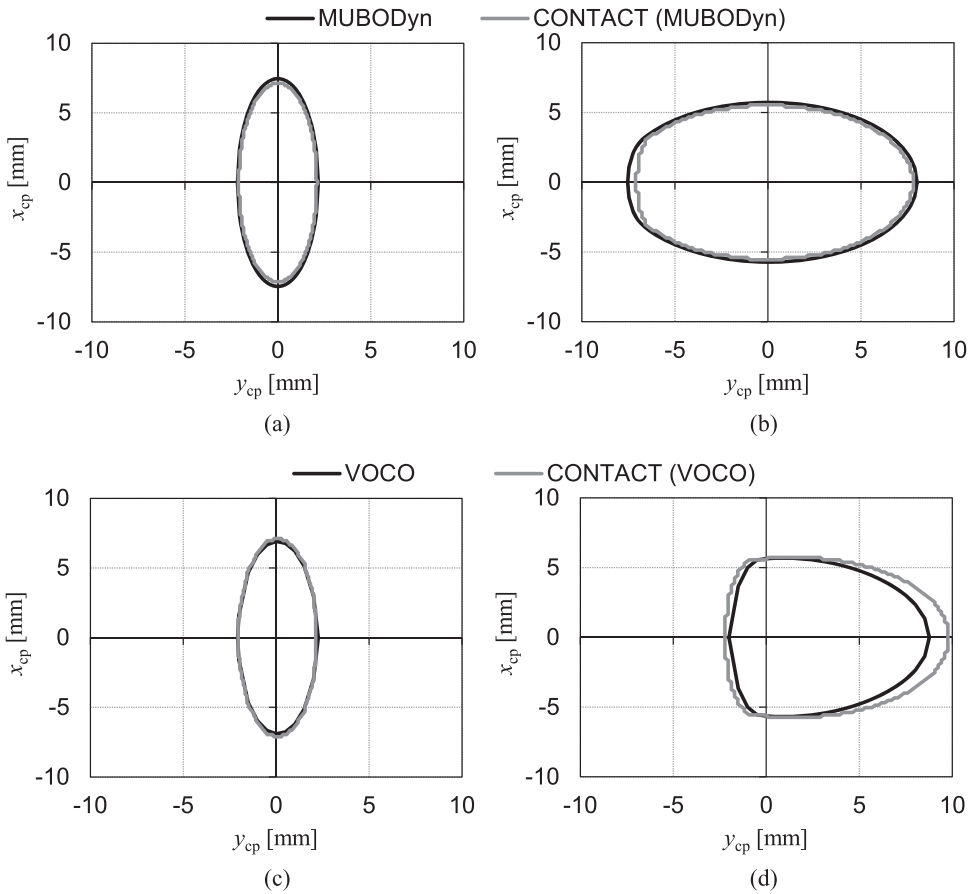
Figure 16. Contact patch of the outer trailing wheel of 'Run 1' obtained with MUBODyn at (a) $s_r = 0$ m and (b) $s_r = 25$ m and with VOCO at (c) $s_r = 0$ m and (d) $s_r = 25$ m.

and normal contact function obtained with MUBODyn and VOCO are used. At the beginning of the curve transition a half elliptical shape is observed in both software, meaning that the contact patch is due to the contact with the sharp edge observed in Figure 18(b), at $u_r = 0$ mm. Hence, the maximum penetration is observed near the sharp edge, which leads to an extreme contact where high contact pressures are expected. The normal pressure distribution across the contact patch has been determined with CONTACT for the contact conditions of MUBODyn and VOCO and displayed in Figure 21. A very high normal pressure is observed, between 3 and 12 GPa, that would lead to plastic deformation of the wheel and rail and, in the case of rail, the sharp edge would be smoothed after one wheel passage.

When the wheel reaches the end of the curve transition, the contact patches increase in both MUBODyn and VOCO, assuming a portion of an ellipse, as observed in Figure 19(b–d). The discrepancy between VOCO and CONTACT in the contact surface at the end of the transition curve is due to the smoothing of the B curvature inherent to the STRIPES method [38], which is discussed in section 2. Using the non-smoothed curvature leads to better results in terms of contact surface but the abrupt change of curvature at $y_r = 0$
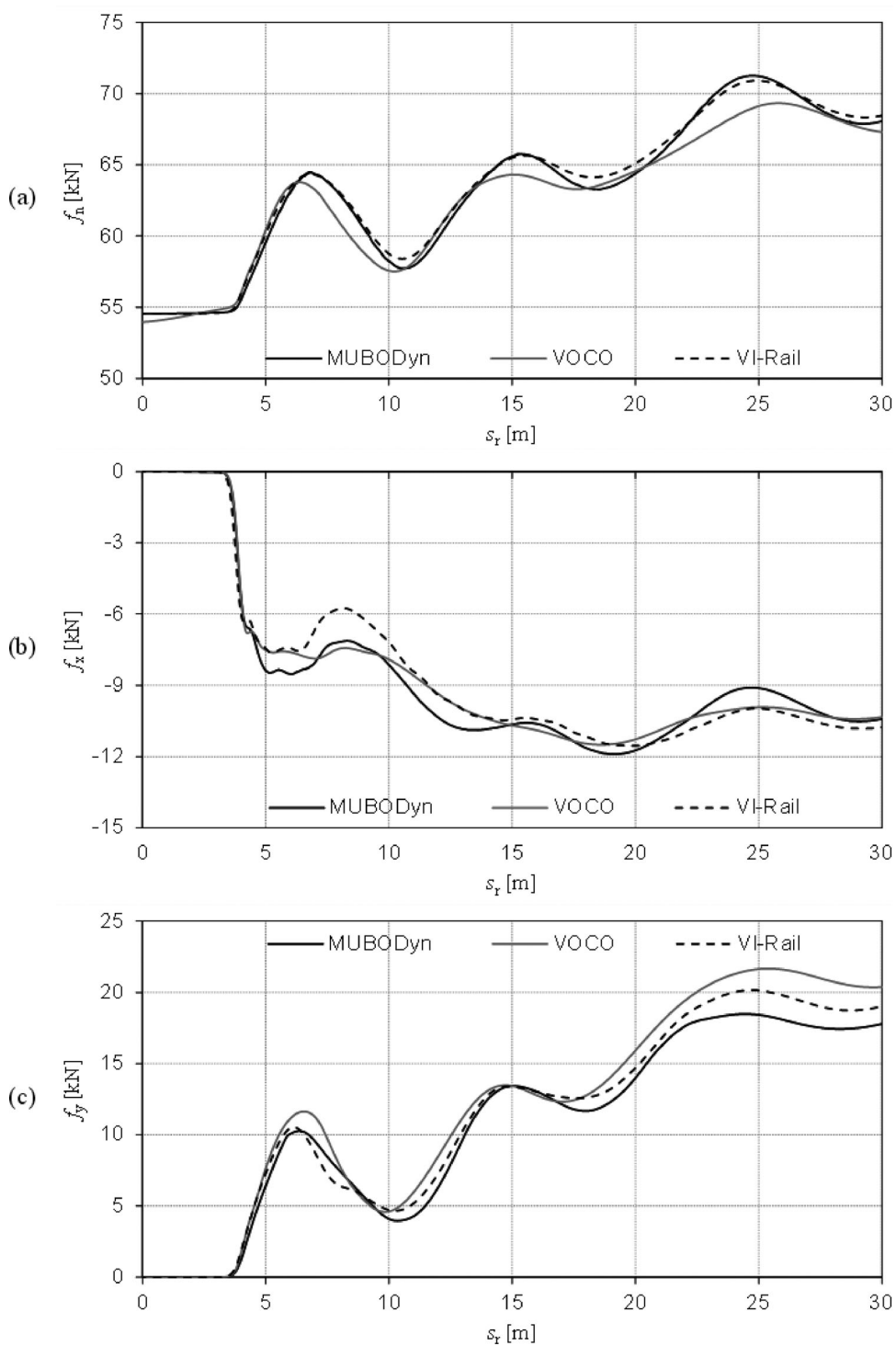
Figure 17. (a) Normal contact force (b) Longitudinal creep force and (c) Lateral creep force obtained for the outer trailing wheel.
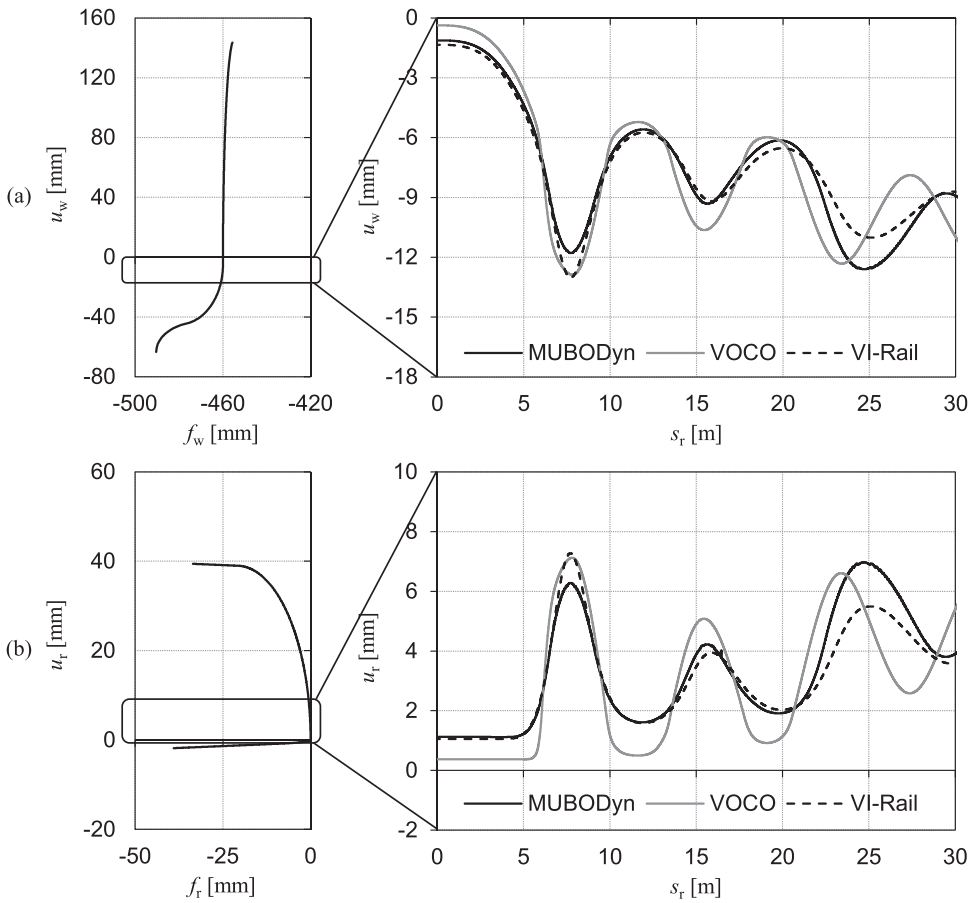
Figure 18. Left hand side: (a) Wheel and (b) rail profiles. Right hand side: corresponding position of the contact patch for the trailing outer wheel-rail pair.

leads to a sharp variation in the contact patch, as shown in Figure 20(b). The smoothed curvature shown in Figure 20(a) leads to higher contact stiffness k_i hence resulting in a smaller contact patch. Trimming the profile so as to remove the sharp edge leads to more consistent results with the other methods. The sharp edge presents a situation where any method using the half space assumption is challenged and, therefore, the results must be carefully interpreted.

The contact forces of the trailing outer wheel contact patch are displayed in Figure 22. A better agreement is observed between MUBODyn and VI-Rail, where the discrepancies with VOCO are related to the difficulties at coping with the sharp edge. Another issue is faced by MUBODyn that leads to high frequency oscillations that are observed at the peaks of the contact force, as highlighted in Figure 22(a), which is caused by difficulties at determining the contact patch near the sharp edge. In addition, a sudden peak has been obtained with MUBODyn that reaches 95 kN for the normal contact force is a numerical artifact which is caused by a sudden change of the contact position of the rail as highlighted
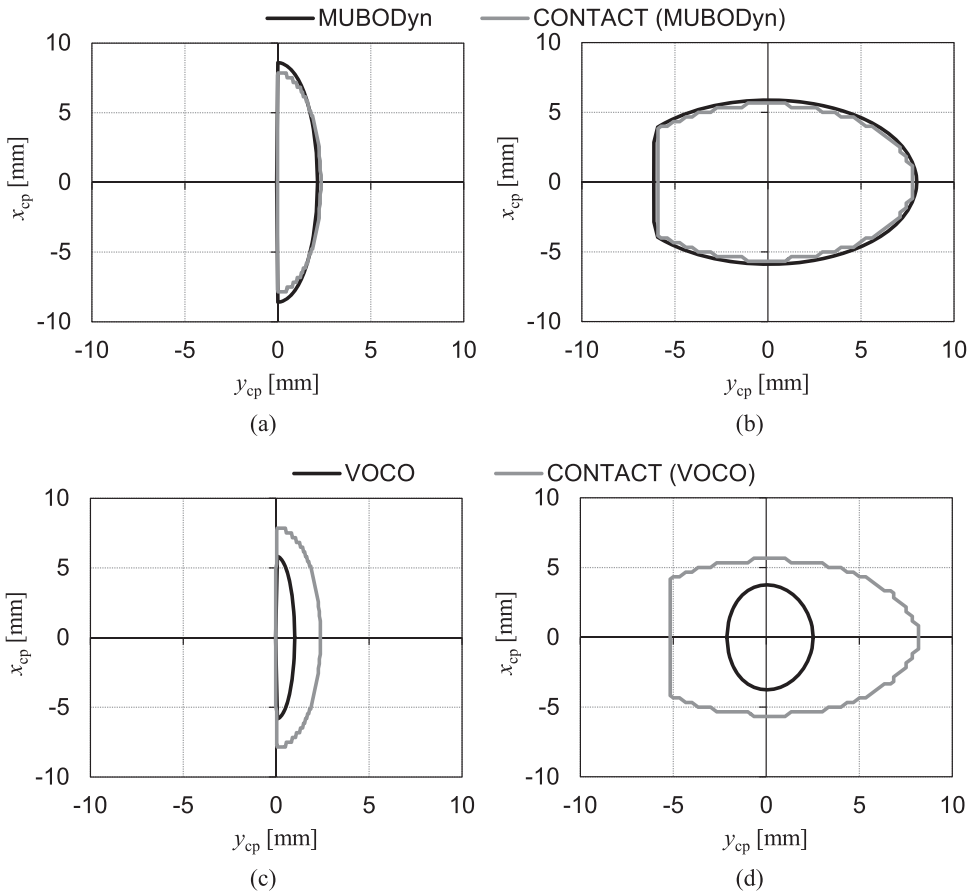
Figure 19. Contact patch of the outer trailing wheel obtained of 'Run 2' with MUBODyn at (a) $s_r = 0$ m and (b) $s_r = 25$ m and with VOCO at (c) $s_r = 0$ m and (d) $s_r = 25$ m.
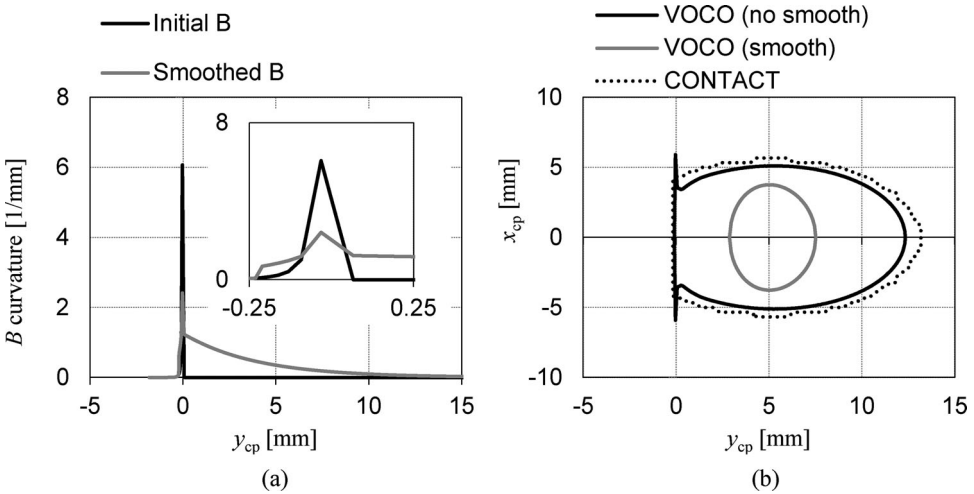

Figure 20. VOCO results at $s_r = 25$ m with and without smoothing of the (a) B curvature and (b) corresponding contact patches including contact patch obtained with CONTACT.
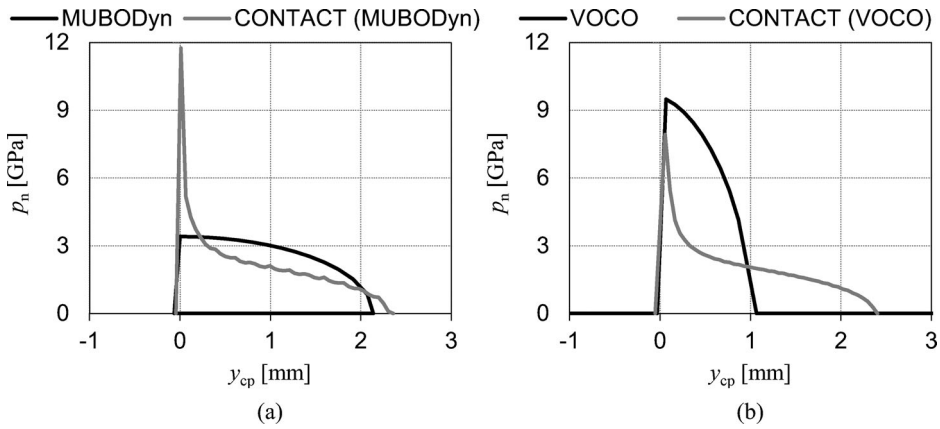
Figure 21. Normal contact pressure with the penetration function obtained with (a) MUBODyn and (b) VOCO for Run 2 at $s_r = 0$ m.

in Figure 18(b). Therefore, the methods currently implemented in MUBODyn to deal with such extreme cases lead to some numerical artifacts.

4.3. Run 3 – impact load

In this case study, the focus is put on the time-history of the normal contact load, where high impact loads are observed. Figure 23 shows the contact position along the crossing element as well as the normal contact forces at intervals identified with numbers '1', '2' and '3'. The contact position deviates laterally from $s_r = 0$ m, which corresponds to the lateral deviation of the wing rail.

The first contact with the crossing nose occurs at around $s_r = 0.92$ m, as observed in plot related with interval '1'. Due to the output time-step, the contact initiation is not well captured in the crossing nose, where the first normal contact force reported on the crossing is higher than 50 kN for the three multibody codes, as shown in Figure 23(b). The same observation is valid for the end of the contact on the wing rail, where the last contact force reported is not null. Regarding the impact force observed in Figure 23(b), a reasonable agreement between the three multibody codes has been obtained, where a better resemblance is observed between MUBODyn and VI-Rail in the first peak that reaches almost 500 kN. In this case, the normal force shows an oscillatory response because, on the one hand, the wheel tends to separate from the rail due to the impact force leading to a decrease of the normal force and, on the other hand, the elevation of the crossing nose increases the interference that ultimately increases the normal force. The three multibody codes use different normal contact force formulations, namely, the energy dissipation at the wheel-rail contact is defined differently, which justifies the discrepancies between the results. Following this first impact load on the nose, the wheel loses contact with the rail momentarily in all three codes.

Figure 23(c) shows the second contact with the crossing nose after a rebound of the wheel occurs at the interval indicated by number '2'. VI-Rail predicts first the contact around $s_r = 1.4$ m, whereas VOCO and MUBODyn around $s_r = 1.6$ m, which represents the end of the crossing. Here, both codes show a first peak at high frequency followed by
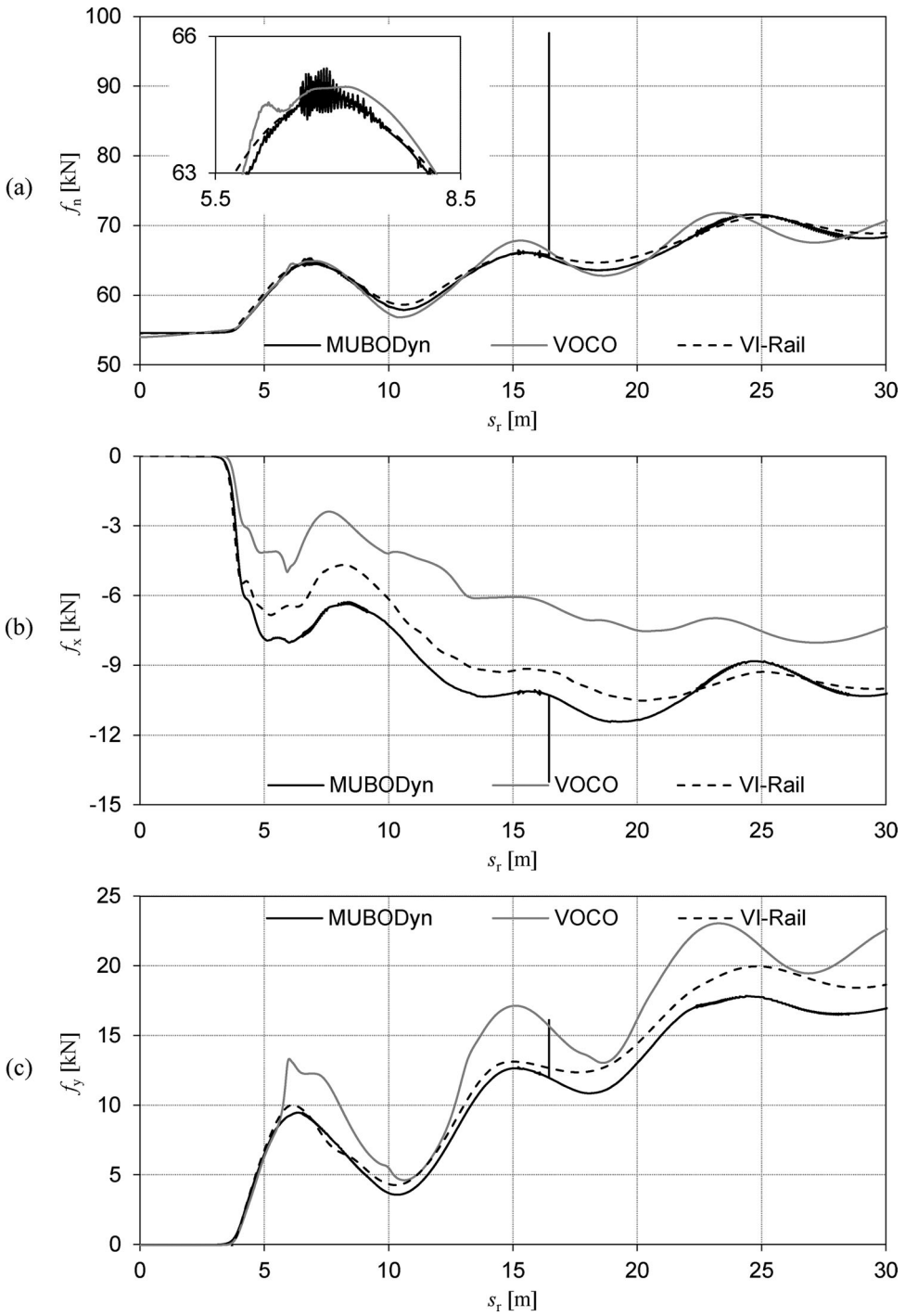
Figure 22. (a) Normal contact force (b) Longitudinal creep force and (c) Lateral creep force obtained for the outer trailing wheel.
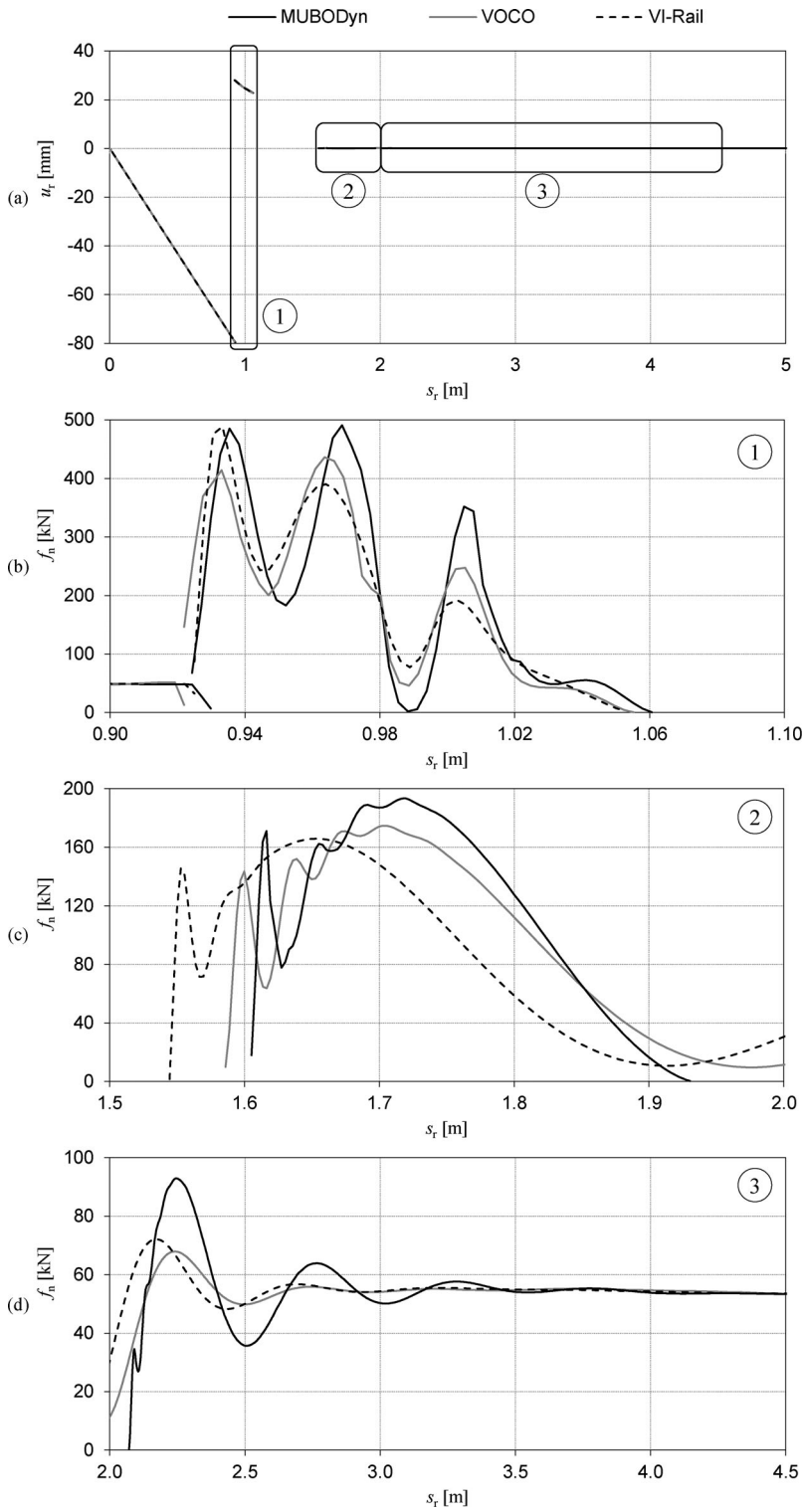
Figure 23. Contact position on the rail surface and normal contact forces at intervals indicated by '1', '2' and '3'.

another peak with lower frequency. In this case, only MUBODyn losses contact a second time, although VI-Rail and VOCO reached normal contact forces lower than 20 kN.

In the interval identified by '3', MUBODyn exhibits the third contact where a first peak of high frequency is observed followed by an oscillatory response that shows slower stabilisation when compared with VOCO and VI-Rail. Therefore, the discrepancies between the normal contact forces are mainly justified by the different strategies to account for the dissipation at the contact force, where MUBODyn uses the restitution coefficient [17,20], VOCO uses a linear damper, and VI-Rail uses a 'Hertz damping ratio', which meaning not clearly explained in the VI-Rail documentation [52].

4.4. Computational efficiency

The average computational time per second of simulation for the scenarios considered in this work are listed in Table 1. MUBODyn shows a high computational effort as its MAT-LAB version has been used in this work, which is at least 10 times slower than its FORTRAN compiled version as tested under normal plain line application. The methodologies used here for S&C are not yet available in a compiled format[61]. In addition, MUBODyn comprises an online contact detection method that involves solving an optimisation problem that is the most time-consuming procedure at any time-step of the simulation. Note that the computational time doubles for Run 2, due to the instabilities observed in Figure 22, that lead to a significant reduction of the variable time-step. VOCO is the fastest out of the three multibody codes, not only because it is coded in FORTRAN, but also because the parameters needed for the contact calculations are pre-tabulated and interpolated online to calculate the contact conditions. The computational effort does not change significantly as a fixed time-step integration method is used, leading to a reasonable similar computational effort. The computational cost of VI-Rail simulations is 2–3 times higher than VOCO, as it is a compiled code and it uses an online contact detection approach that seems to be simpler when compared to that in MUBODyn.

Table 1. Computational time for a second of simulation.

Multibody Code	MUBODyn	VOCO	VI-Rail
Run 1	$\sim$ 0.7 [h/s]	11 [s/s]	$\sim$ 33 [s/s]
Run 2	$\sim$ 1.8 [h/s]	17 [s/s]	$\sim$ 36 [s/s]
Run 3	$\sim$ 0.9 [h/s]	13 [s/s]	$\sim$ 20 [s/s]

5. Conclusions

This work aims to evaluate and critically discuss the implications of the wheel-rail contact methodologies present in different railway multibody dynamics software, namely MUBO-Dyn, VOCO and VI-Rail, on the prediction of the contact forces for highly transient contact conditions, such as those observed in S&C. Three cases have been designed to test specific wheel-rail contact conditions that typically occur in the negotiation of S&C, namely, conformal contact, contact at a sharp edge of a switch rail and impact at a crossing nose. Brief descriptions of the wheel-rail contact models implemented in MUBODyn, VOCO and VI-Rail are provided, which enables to discuss the differences in the results.

The scenarios considered in this work are simple to model, the simplified bogie model and the wheel and rail profiles being defined by few parameters, making these models possible to be replicated by interested readers using other or the same software.

Overall, a reasonable agreement between MUBODyn, VOCO and VI-Rail is observed for the three simulation cases presented in this work for most of the results. All the codes handle the extreme cases considered showing that all tested methods are suitable to handle realistic wheel-rail contact problem in severe transitions. In Run 1, typical wheel-rail contact conditions are observed from which slight discrepancies observed between the software are related to the different methods used to solve the contact detection problem and to determine the contact patch. Higher discrepancies are observed in Run 2, where a contact with a sharp edge is simulated. In this case, an extreme contact condition that would lead to plastic deformation due to the high contact stress is observed, which has led to poor results and numerical instabilities. It should be noted that Run 2 presents a case where the half space assumption used in all the methods discussed is violated and hence the results should be interpreted accordingly. The contact patches of Runs 1 and 2 have been compared with the reference CONTACT software, showing good agreement with MUBODyn. In Run 3, the impact force has been studied in detail. Two impact behaviours have been obtained with the three multibody codes. The normal force presents an oscillatory behaviour with high frequency on the crossing nose, while the other impacts observed on the nominal rails comprises an initial short peak of force with a high frequency that is followed by an oscillatory behaviour with lower frequency, similar to the P1 and P2 forces stated in Jenkins work [62]. The observed discrepancies between the codes are due to the normal contact models implemented in the three multibody codes that capture the restitution effect differently. MUBODyn uses a normal contact model for impact loads [17], in which the restitution coefficient is explicitly used, VOCO uses a linear damper, while the method used in VI-Rail is not disclosed in its documentation. Due to the simplicity of the crossing model, the performance of the rail interpolation did not show to have any impact on the results. In terms of computational efficiency, VOCO took seconds to run all simulations, while VI-Rail took minutes and MUBODyn hours. Several factors affect the computational performance of the codes. MUBODyn uses an interpreted programming language rather than a compiled programming language, which at present significantly affect its speed. It also uses an advanced and time-consuming method to solve the contact detection problem while applying online contact calculation alike VI-Rail. The pre-tabulation of the contact parameters would appear to be one significant reason making VOCO the fastest code.

The wheel-rail contact modelling is a challenging topic that requires further research to improve accuracy while expanding the conditions for which wheel-rail contact models provide realistic results. The implementation of wheel-rail contact models in a multibody code is also a crucial research topic as different approaches impact the wheel-rail contact forces and lead to varying computational efficiency, as demonstrated in this work. Suggestions for the enhancement of wheel-rail contact models are drawn from this work, namely, to deal with S&C. One is the determination of the contact patch in cases where the half space assumption is not valid, as shown in the 'Run 2'. Additionally, determining asymmetric contact patches has been highlighted in other works when the yaw angle is higher [63,64]. For rails with variable cross sections, this might play a role even for small yaw angles. Also, in 'Run 2' high normal pressure is obtained from which plastic deformation would occur, which recalls the suggestions presented in [40,41] where the consideration

of plasticity on the normal and tangential contact must be considered when focusing the wheel-rail interaction. Acknowledging the continuous development of many wheel-rail contact forces [18], many are appropriately developed for steady state conditions. However, for transient contact conditions, as it occurs when the wheel load transfer from one rail to another, few works have explicitly identified a formulation to deal with the restitution effect [17,20,65]. Complementary, the integration method to perform the dynamic analysis need to be correctly chosen, where variable time-step integration algorithms are preferred, and the high frequency contents are adequately captured. In the range of high frequency, the system structural deformation can play a role in the wheel-rail interaction as demonstrated in many works [66,67].

Acknowledgements

Disclosure statement

No potential conflict of interest was reported by the author(s).

Funding

ORCID

H. Magalhaes http://orcid.org/0000-0001-7070-7958
F. Marques http://orcid.org/0000-0002-1162-5618
P. Antunes http://orcid.org/0000-0001-6910-8456
P. Flores http://orcid.org/0000-0002-7013-4202
J. Pombo http://orcid.org/0000-0002-5877-1989
J. Ambrósio http://orcid.org/0000-0001-6681-5657
A. Qazi http://orcid.org/0000-0002-4636-0103
M. Sebes http://orcid.org/0000-0002-8358-152X
Y. Bezin http://orcid.org/0000-0002-0599-8696

References

[1] Wan C, Markine V, Dollevoet R. Robust optimisation of railway crossing geometry. Veh Syst Dyn. 2016;54:617–637. doi:10.1080/00423114.2016.1150495.
[2] Costa N, Antunes J, Magalhães P, et al. A finite element methodology to model flexible tracks with arbitrary geometry for railway dynamics applications. Comput Struct. 2021;254:106519. doi:10.1016/j.compstruc.2021.106519.

[3] Olivier B, Verlinden O, Kouroussis G. Effect of applied force cosimulation schemes on recoupled vehicle/track problems. Multibody Syst Dyn. 2020;50:337–353. doi:10.1007/s11044-020-09748-8.

[4] Funfschilling C, Perrin G, Sebes M, et al. Probabilistic simulation for the certification of railway vehicles. Proc Inst Mech Eng Part F J Rail Rapid Transit. 2015;229:770–781. doi:10.1177/0954409715589395.

[5] Magalhães H, Ambrósio J, Pombo J. Railway vehicle modelling for the vehicle–track interaction compatibility analysis. Proc Inst Mech Eng Part K J Multi-Body Dyn. 2016;230:251–267. doi:10.1177/1464419315608275.

[6] Pagaimo J, Magalhães H, Costa JN, et al. Derailment study of railway cargo vehicles using a response surface methodology. Veh Syst Dyn. 2020: 1–26. doi:10.1080/00423114.2020.1815810.

[7] Enblom R. Deterioration mechanisms in the wheel–rail interface with focus on wear prediction: a literature review. Veh Syst Dyn. 2009;47:661–700. doi:10.1080/00423110802331559.

[8] Johansson A, Pålsson B, Ekh M, et al. Simulation of wheel–rail contact and damage in switches & crossings. Wear. 2011;271:472–481. doi:10.1016/j.wear.2010.10.014.

[9] Pombo J, Ambrósio J, Pereira M, et al. Development of a wear prediction tool for steel railway wheels using three alternative wear functions. Wear. 2011;271:238–245. doi:10.1016/j.wear.2010.10.072.

[10] Magalhães H, Madeira JFA, Ambrósio J, et al. Railway vehicle performance optimisation using virtual homologation. Veh Syst Dyn. 2016;54:1177–1207. doi:10.1080/00423114.2016.1196821.

[11] Ye Y, Sun Y, Dongfang S, et al. Optimizing wheel profiles and suspensions for railway vehicles operating on specific lines to reduce wheel wear: a case study. Multibody Syst Dyn. 2021;51:91–122. doi:10.1007/s11044-020-09722-4.

[12] Magalhães H, Pombo J, Ambrósio J, et al. Rail vehicle design optimization for operation in a mountainous railway track. Innov Infrastruct Solut. 2017;2:31. doi:10.1007/s41062-017-0088-1.

[13] Kalker JJ. Three-Dimensional Elastic Bodies in rolling contact. Dordrecht: Kluwer Academic Publishers; 1990.

[14] Xu L, Zhang Q, Yu Z, et al. Vehicle–track interaction with consideration of rail irregularities at three-dimensional space. J Vib Control. 2020;26:1228–1240. doi:10.1177/1077546319894816.

[15] Ren Z, Sun S, Xie G. A method to determine the two-point contact zone and transfer of wheel–rail forces in a turnout. Veh Syst Dyn. 2010;48:1115–1133. doi:10.1080/00423110903337281.

[16] Falomi S, Malvezzi M, Meli E. Multibody modeling of railway vehicles: innovative algorithms for the detection of wheel–rail contact points. Wear. 2011;271:453–461. doi:10.1016/j.wear.2010.10.039.

[17] Marques F, Magalhães H, Pombo J, et al. A three-dimensional approach for contact detection between realistic wheel and rail surfaces for improved railway dynamic analysis. Mech Mach Theory. 2020;149:103825. doi:10.1016/j.mechmachtheory.2020.103825.

[18] Meymand SZ, Keylin A, Ahmadian M. A survey of wheel–rail contact models for rail vehicles. Veh Syst Dyn. 2016;54:386–428. doi:10.1080/00423114.2015.1137956.

[19] Qazi A, Yin H, Sebès M, et al. A semi-analytical numerical method for modelling the normal wheel–rail contact. Veh Syst Dyn. 2020: 1–19. doi:10.1080/00423114.2020.1854319.

[20] Magalhães H, Marques F, Liu B, et al. Implementation of a non-Hertzian contact model for railway dynamic application. Multibody Syst Dyn. 2020;48:41–78. doi:10.1007/s11044-019-09688-y.

[21] Iwnicki S. Manchester benchmarks for rail vehicle simulation. Veh Syst Dyn. 1998;30; doi:10.1080/00423119808969454.

[22] Shackleton P, Iwnicki S. Comparison of wheel–rail contact codes for railway vehicle simulation: an introduction to the Manchester contact benchmark and initial results. Veh Syst Dyn. 2008;46:129–149. doi:10.1080/00423110701790749.

[23] Vollebregt EAH, Iwnicki SD, Xie G, et al. Assessing the accuracy of different simplified frictional rolling contact algorithms. Veh Syst Dyn. 2012;50:1–17. doi:10.1080/00423114.2011.552618.

[24] Liu B, Bruni S. Influence of individual wheel profiles on the assessment of running dynamics of a rail vehicle by numerical simulation: a case study. 2021. doi:10.1080/00423114.2021.1901940.

[25] Burgelman N, Sichani MS, Enblom R, et al. Influence of wheel-rail contact modelling on vehicle dynamic simulation. Veh Syst Dyn. 2015;53:1190–1203. doi:10.1080/00423114.2015.1039550.

[26] Bezin Y, Pålsson BA, Kik W, et al. Multibody simulation benchmark for dynamic vehicle–track interaction in switches and crossings: results and method statements. Veh Syst Dyn. 2021: 1–38. doi:10.1080/00423114.2021.1959038.

[27] Sebes M, Ayasse JB, Chollet H, et al. Application of a semi-Hertzian method to the simulation of vehicles in high-speed switches. Veh Syst Dyn. 2006;44:341–348. doi:10.1080/00423110600871533.

[28] Alfi S, Bruni S. Mathematical modelling of train-turnout interaction. Veh Syst Dyn. 2009;47:551–574. doi:10.1080/00423110802245015.

[29] Bezin Y, Sarmiento-Carnevali ML, Sichani MS, et al. Dynamic analysis and performance of a repoint track switch. Veh Syst Dyn. 2020;58:843–863. doi:10.1080/00423114.2019.1612925.

[30] Kalker JJ. Survey of wheel-rail rolling contact theory. Veh Syst Dyn. 1979;8:317–358.

[31] Piotrowski J, Chollet H. Wheel–rail contact models for vehicle system dynamics including multi-point contact. Veh Syst Dyn. 2005;43:455–483. doi:10.1080/00423110500141144.

[32] Bruni S, Meijaard JP, Rill G, et al. State-of-the-art and challenges of railway and road vehicle dynamics with multibody dynamics approaches. The Author(s) (2020).

[33] Vollebregt E. Detailed wheel/rail geometry processing with the conformal contact approach. Multibody Syst Dyn. 2020. doi:10.1007/s11044-020-09762-w.

[34] Vollebregt EAH. Detailed wheel/rail geometry processing using the planar contact approach. Veh Syst Dyn. 2020: 1–39. doi:10.1080/00423114.2020.1853180.

[35] Shabana AA, Tobaa M, Sugiyama H, et al. On the computer formulations of the wheel/rail contact problem. Nonlinear Dyn. 2005;40:169–193. doi:10.1007/s11071-005-5200-y.

[36] Escalona JL, Aceituno JF, Urda P, et al. Railway multibody simulation with the knife-edge-equivalent wheel–rail constraint equations. Multibody Syst Dyn. 2020;48:373–402. doi:10.1007/s11044-019-09708-x.

[37] Aceituno JF, Urda P, Briales E, et al. Analysis of the two-point wheel-rail contact scenario using the knife-edge-equivalent contact constraint method. Mech Mach Theory. 2020;148:103803. doi:10.1016/j.mechmachtheory.2020.103803.

[38] Ayasse J, Chollet H. Determination of the wheel rail contact patch in semi-Hertzian conditions. Veh Syst Dyn. 2005;43:161–172. doi:10.1080/00423110412331327193.

[39] Piotrowski J, Kik W. A simplified model of wheel/rail contact mechanics for non-Hertzian problems and its application in rail vehicle dynamic simulations. Veh Syst Dyn. 2008;46:27–48. doi:10.1080/00423110701586444.

[40] Sebès M, Chevalier L, Ayasse J-B, et al. A fast-simplified wheel–rail contact model consistent with perfect plastic materials. Veh Syst Dyn. 2012;50:1453–1471. doi:10.1080/00423114.2012.669483.

[41] Sebès M, Chollet H, Ayasse J-B, et al. A multi-Hertzian contact model considering plasticity. Wear. 2014;314:118–124. doi:10.1016/j.wear.2013.11.036.

[42] Sh. Sichani M, Enblom R, Berg M. A novel method to model wheel-rail normal contact in vehicle dynamics simulation. Veh Syst Dyn. 2014;52:1752–1764. doi:10.1080/00423114.2014.961932.

[43] Sh. Sichani M, Enblom R, Berg M. An alternative to FASTSIM for tangential solution of the wheel–rail contact. Veh Syst Dyn. 2016;54:748–764. doi:10.1080/00423114.2016.1156135.

[44] Sugiyama H, Tanii Y, Matsumura R. Analysis of wheel/rail contact geometry on railroad turnout using longitudinal interpolation of rail profiles. J Comput Nonlinear Dyn. 2011;6:1–5. doi:10.1115/1.4002342.

[45] Sugiyama H, Sekiguchi T, Matsumura R, et al. Wheel/rail contact dynamics in turnout nego-
tiations with combined nodal and non-conformal contact approach. Multibody Syst Dyn.
2012;27:55–74. doi:10.1007/s11044-011-9252-0.

[46] Hamper MB, Wei C, Shabana AA. Use of ANCF surface geometry in the rigid body contact
problems: application to railroad vehicle dynamics. J Comput Nonlinear Dyn 2015;10:021008,
doi:10.1115/1.4027442.

[47] Pålsson BA, Nielsen JCO. Track gauge optimisation of railway switches using a genetic
algorithm. Veh Syst Dyn. 2012;50:365–387. doi:10.1080/00423114.2012.665167.

[48] Hamarat M, Kaewunruen S, Papaelias M, et al. New insights from multibody dynamic analyses
of a turnout system under impact loads. Appl Sci. 2019;9:4080), doi:10.3390/app9194080.

[49] Wiest M, Kassa E, Daves W, et al. Assessment of methods for calculating contact pressure in
wheel-rail/switch contact. Wear. 2008;265:1439–1445. doi:10.1016/j.wear.2008.02.039.

[50] Ma X, Wang P, Xu J, et al. Numerical simulation of rail surface-initiated rolling contact fatigue
in the switch panel of railway turnouts. Proc Inst Mech Eng Part F J Rail Rapid Transit.
2020;0:1–11. doi:10.1177/0954409720909971.

[51] Ma X, Wang P, Xu J, et al. Assessment of non-Hertzian wheel-rail contact models for numerical
simulation of rail damages in switch panel of railway turnout. Wear. 2019;432–433:102912,
doi:10.1016/j.wear.2019.05.027.

[52] VI-Grade: VI-Rail Documentation, (2019).

[53] Sun Y, Zhai W, Guo Y. A robust non-Hertzian contact method for wheel–rail normal contact
analysis. Veh Syst Dyn. 2018;56:1899–1921. doi:10.1080/00423114.2018.1439587.

[54] Sichani MS, Enblom R, Berg M. Comparison of non-elliptic contact models: towards fast and
accurate modelling of wheel–rail contact. Wear. 2014;314:111–117. doi:10.1016/j.wear.2013.11.
047.

[55] Johnson KL. Contact mechanics. Cambridge: Cambridge University Press; 1985.

[56] Polach O. A fast wheel-rail forces calculation computer code. Veh Syst Dyn. 1999;33:728–739.
doi:10.1080/00423114.2013.826370.

[57] Qazi A, Sebès M, Chollet H, et al. An extension of FASTSIM for steady state non-Hertzian
contact). The 27th IAVSD symposium on dynamics of vehicles on roads and tracks; Aug 2021;
Saint-Petersburg, Russia. 2021.

[58] Iwnick DS. Manchester benchmarks for rail vehicle simulation. Veh Syst Dyn. 1998;30:
295–313. doi:10.1080/00423119808969454.

[59] Vollebregt E. User guide for CONTACT, rolling and sliding contact with friction, (2020).

[60] Kalker JJ. Three-Dimensional Elastic Bodies in rolling contact. Dordrecht: Springer Nether-
lands; 1990.

[61] Ambrósio J, Pombo J. A unified formulation for mechanical joints with and without clear-
ances/bushings and/or stops in the framework of multibody systems. Multibody Syst Dyn.
2018;42:317–345. doi:10.1007/s11044-018-9613-z.

[62] Jenkins HH, Stephenson JE, Clayton GA, et al. The effect of track and vehicle parameters on
wheelrail vertical dynamic forces. Railw Eng J. 1974;3.

[63] Liu B, Bruni S, Vollebregt E. A non-Hertzian method for solving wheel–rail normal con-
tact problem taking into account the effect of yaw. Veh Syst Dyn. 2016;54:1226–1246.
doi:10.1080/00423114.2016.1196823.

[64] Yunguang Y, Sun Y, Shi D, et al. A wheel wear prediction model of non-Hertzian wheel-rail
contact considering wheelset yaw: comparison between simulated and field test results. (2021).

[65] Pombo J, Ambrósio J, Silva M. A new wheel–rail contact model for railway dynamics. Veh Syst
Dyn. 2007;45:165–189. doi:10.1080/00423110600996017.

[66] Kaiser I. Refining the modelling of vehicle–track interaction. Veh Syst Dyn. 2012;50:229–243.
doi:10.1080/00423114.2012.671948.

[67] Kaiser I, Poll G, Vinolas J. Modelling the impact of structural flexibility of wheelsets and rails
on the wheel-rail contact and the wear. Wear. 2020: 203445), doi:10.1016/j.wear.2020.203445.

Appendix A

Table 2. Bogie model parameters.

-	Properties	Values	Units
m_w	Mass of the wheelset	1813	[kg]
$I_{w,roll}$	Roll moment of inertia of the wheelset	1120	[kg.m^2]
$I_{w,pitch}$	Pitch moment of inertia of the bogie wheelset	112	[kg.m^2]
$I_{w,yaw}$	Yaw moment of inertia of the bogie wheelset	1120	[kg.m^2]
z_w	Height and nominal radius of the wheelset	0.460	[m]
m_b	Mass of the bogie frame	18615	[kg]
$I_{b,roll}$	Roll moment of inertia of the bogie frame	1722	[kg.m^2]
$I_{b,pitch}$	Pitch moment of inertia of the bogie frame	1476	[kg.m^2]
$I_{b,yaw}$	Yaw moment of inertia of the bogie frame	3067	[kg.m^2]
z_b	Height of the bogie frame	0.600	[m]
L_w	Distance between wheelsets	2.560	[m]
L_a	Half distance between axleboxes	1.000	[m]
k_x	Longitudinal stiffness	31.391	[MN/m]
c_x	Longitudinal damping	15.000	[kN.s/m]
L_x	Length of the longitudinal spring	0.450	[m]
k_y	Lateral stiffness	3.884	[MN/m]
c_y	Lateral damping	2.000	[kN.s/m]
L_y	Length of the lateral spring	0.400	[m]
k_z	Vertical stiffness	1.220	[MN/m]
c_z	Vertical damping	4.000	[kN.s/m]
L_z	Deformed (undeformed) length of the vertical spring	0.420 (0.457421)	[m]

Table 3. Parameters of the co-running model shown in Figure 9(b).

-	Properties	Values	Units
m_r	Mass of the rail	60	[kg]
m_s	Mass of the sleeper-ballast	1400	[kg]
$I_{s,roll}$	Roll moment of inertia of the sleeper-ballast	450	[kg.m^2]
D	Distance between rails	1.500	[m]
$k_{p,y}$	Lateral stiffness of the pad	30	[N/m]
$c_{p,y}$	Lateral damping of the pad	150	[N.s/m]
$k_{p,z}$	Vertical stiffness of the pad	150	[MN/m]
$c_{p,z}$	Vertical damping of the pad	100	[kN.s/m]
$k_{s,y}$	Lateral stiffness of the sleeper-ballast	70	[N/m]
$c_{s,y}$	Lateral damping of the sleeper-ballast	350	[N.s/m]
$k_{s,y}$	Vertical stiffness of the sleeper-ballast	140	[MN/m]
$c_{s,y}$	Vertical damping of the sleeper-ballast	1400	[kN.s/m]

Table 4. Wheel parameters for Runs 1, 2 and 3.

	Properties	Runs 1, 2 and 3	Units
R_0	Nominal wheel radius	0.460	[m]
Δs_w	Distance between points of the wheel profile	0.0005	[m]
a_T	Vertical semi axis of the tread ellipse	0.005	[m]
b_T	Horizontal semi axis of the tread ellipse	0.150	[m]
a_C	Vertical semi axis of the concave ellipse	0.020	[m]
b_C	Horizontal semi axis of the concave ellipse	0.040	[m]
a_F	Vertical semi axis of the flange ellipse	0.020	[m]
b_F	Horizontal semi axis of the flange ellipse	0.020	[m]
u_0	Lateral coordinate of the tread-concave ellipses union	−0.005	[m]
df_w	Wheel slope at the flange-concave ellipses union	3	[-]

Table 5. Rail parameters for Runs 1, 2 and 3 (∗the right rail of Run 3 also comprises a set of profiles that represent the crossing).

	Property	Run 1 and 3 (both rails∗)	Run 2 (left rail)	Run 2 (right rail)	Units
f_0	Height of the rail profile	0.000	0.000	0.000	[m]
Δs_r	Distance between points of the rail profile	0.0005	0.0001	0.0001	[m]
a_L	Vertical semi axis of the left ellipse	0.021	0.021	0.021	[m]
b_L	Horizontal semi axis of the left ellipse	0.039	0.039	0.001	[m]
df_L	Slope of the left straight line	30	30	30	[-]
Δu_L	Width of the left straight line	0.001	0.001	0.001	[m]
a_R	Vertical semi axis of the right ellipse	0.021	0.021	0.021	[m]
b_R	Horizontal semi axis of the right ellipse	0.039	0.001	0.039	[m]
df_R	Slope of the right straight line	30	30	30	[-]
Δu_R	Width of the right straight line	0.001	0.001	0.001	[m]

Table 6. Crossing parameters.

-	Properties	Values	Units
Δp	Distance between rail profiles	0.01	[m]
Δs_r	Distance between points of the crossing profile	0.0005	[m]
f_0	Heigh of the rail	0	[m]
a_r	Vertical semi axis of the ellipse	0.021	[m]
b_r	Horizontal semi axis of the ellipse	0.039	[m]
df_r	Slope of the straight line	30	[-]
Δu_r	Width of the straight line	0.001	[m]
α	Crossing angle	5	[°]
β	Longitudinal angle of the crossing nose	4	[°]
h_N	Height difference between the nose and wing rails at position '2'	0.025	[m]
a_N	Vertical semi axis of the ellipse of the nose	0.002	[m]
b_N	Horizontal semi axis of the ellipse of the nose	0.002	[m]
c	Distance between crossing nose and wing rail	0.050	[m]